Neuromuscular Basis of *Drosophila* Larval Escape Behavior

Patricia C. Cooney[1,2], Wenze Li[3,4,§], Yuhan Huang [5,6,§], Richard Hormigo[1], Tanya Tabachnik[1], Elizabeth M.C. Hillman[3,7,8,9], Wesley B. Grueber[1,2,10,*], Aref A Zarin[5,6,*,#]

[1] Mortimer B. Zuckerman Mind Brain Behavior Institute, Jerome L. Greene Science Center, 3227 Broadway, L9-007, New York, NY 10027, USA

[2] Department of Neuroscience, Jerome L. Greene Science Center, 3227 Broadway, L9-007, New York, NY 10027, USA

[3] Laboratory for Functional Optical Imaging, Mortimer B. Zuckerman Mind Brain Behavior Institute, Columbia University, New York, NY 10027, USA

[4] Department of Electrical Engineering, Columbia University, New York, NY 10027, USA

[5] Department of Biology, Texas A&M University, College Station, TX 77843, USA

[6] Texas A&M Institute for Neuroscience, Texas A&M University, College Station, TX 77843, USA.

[7] Department of Biomedical Engineering, Columbia University, New York, NY 10027, USA

[8] Department of Radiology, Columbia University Irving Medical Center, New York, NY 10032, USA

[9] Kavli Institute for Brain Science, Columbia University, New York, NY 10032, USA

[10] Department of Physiology and Cellular Biophysics, Jerome L. Greene Science Center, 3227 Broadway, L9-007, New York, NY 10027, USA

[§] equal contributors

[#] Lead Contact
*Correspondence: azarin@bio.tamu.edu (A.A.Z.), wg2135@columbia.edu (W.B.G.)

Author Contributions: *Conceptualization* - P.C.C., W.B.G., and A.A.Z. *Data curation* - P.C.C., W.L., Y.H., E.M.C.H., and A.A.Z. *Formal* Analysis - P.C.C., Y.H., and A.A.Z *Funding Acquisition* – P.C.C., E.M.C.H., W.B.G., and A.A.Z. *Investigation* – P.C.C., W.L., Y.H., and A.A.Z. *Methodology* – P.C.C., W.L., Y.H., R.H., T.T., E.M.C.H., W.B.G., and A.A.Z. *Project Administration* – P.C.C., W.B.G., E.M.C.H., and A.A.Z. *Resources* - P.C.C., W.L., Y.H., R.H., T.T., E.M.C.H., W.B.G., and A.A.Z. *Software* - P.C.C., W.L., and E.M.C.H. *Supervision* – W.B.G., E.M.C.H., and A.A.Z. *Validation* – P.C.C., W.L., Y.H., E.M.C.H., W.B.G., and A.A.Z. *Visualization* - P.C.C., Y.H., W.B.G., and A.A.Z. *Writing, original draft* - P.C.C., W.B.G., and A.A.Z. *Writing, review & editing* - P.C.C., W.L., E.M.C.H., W.B.G., and A.A.Z.

Competing Interest Statement: The authors declare no competing interest.

Classification: BIOLOGICAL SCIENCES-Neuroscience

Key words: Escape Locomotion, premotor-motor-muscle connectome, Motor Circuits, Nociception, *Drosophila* larvae

This PDF file includes:

Main Text

Figures 1 to 4

Abstract

When threatened by dangerous or harmful stimuli, animals engage in diverse forms of rapid escape behavior. In *Drosophila* larvae, escape behavior is characterized by C-shaped bending and lateral rolling, followed by rapid forward crawling. The sensory circuitry that promotes escape has been extensively characterized, but the motor programs underlying escape are unknown. Here, we characterize the neuromuscular basis of escape. We use high-speed, volumetric, Swept Confocally-Aligned Planar Excitation (SCAPE) microscopy to image muscle activity during larval rolling. Unlike the sequential peristaltic muscle contractions from segment to segment that underlie forward and backward crawling, muscle activity progresses in a circumferential sequence during bending and rolling. Certain muscle subgroups show functional antagonism during bending and rolling. We use EM connectome data to identify premotor to motor connectivity patterns that could drive rolling behavior, and test the necessity of specific groups of motor neurons in rolling using neural silencing approaches. Our data reveal the body-wide muscle activity patterns and putative premotor circuit organization for escape.

Significance Statement

To escape from dangerous stimuli, animals execute escape behaviors that are fundamentally different from normal locomotion. The escape behavior of Drosophila larvae consists of C-shaped bending and rolling followed by fast forward crawling. However, the muscle contraction patterns that lead to rolling are poorly understood. We find that following the initial body bending, muscles contract in a circumferential wave around the larva as they enter the bend, maintaining unidirectional rolling that resembles cylinder rolling on a surface. We study the structure of motor circuits for rolling, inhibit different motor neurons to determine which muscles are essential or dispensable for rolling, and propose a circuit model for roll generation. Our findings provide insights into how motor circuits produce diverse motor behaviors.

Introduction

Early in the evolution of animals, nervous systems specialized to permit locomotion[1]. While locomotion supports multiple aspects of evolutionary success (*e.g.* allocating resources, finding mates), one of the most critical of these is escape: the transformation of sensory input into motor output to avoid imminent danger[2–4]. Escape behaviors are rapid and stereotyped yet must be flexible enough to allow animals to evade multiple sources of harm and readjust when danger subsides[3,5,6]. Escape behaviors across species often differ fundamentally from exploratory locomotion[3,7–11].This specificity suggests that dedicated neural circuits or unique activity patterns within shared locomotor circuits are employed during escape. While many studies have investigated how sensory input promotes escape[2,3,6,8,9,12–16], the neuromuscular activity that generates escape movements have been characterized in few model organisms[8,12,17,18]. Furthermore, the model systems in which escape movement generation has been studied have yielded limited understanding of how the sensory circuits that promote escape drive motor circuits. By characterizing escape motor circuits in the *Drosophila* model, with its well-studied sensory system and nearly complete connectome, we aim to understand how sensory input is transformed into motor output during escape.

The *Drosophila* larval body consists of twelve segments, with abdominal segments containing up to 60 different muscles[19]. Forward crawling consists of sequential segmental contractions that propagate from posterior to anterior segments and engages all muscles[19–21]. Upon experiencing harmful mechanical touch or heat, larvae initiate a nocifensive escape consisting of C-shaped bending, rolling, and rapid forward crawling[22]. Rolling causes fast lateral motion—which is faster than escape crawling alone, and can dislodge attacking parasitoid wasps[23,24]. This behavior is initiated by activity of class IV (cIV) dendritic arborization neurons, polymodal nociceptors that tile the body wall[23,25]. Several downstream partners of cIV neurons have been identified and reconstructed using serial transmission electron microscopy[26–30]. Activation of any of several interneurons that are downstream of cIV neurons is sufficient to evoke escape[26–28], but how these interneurons drive downstream motor activity patterns remains poorly characterized.

Despite progress in understanding nociceptive circuitry, characterizing neural and muscular activity during escape behavior presents challenges. In contrast to crawling, rolling behavior is asymmetric, with larvae rolling laterally in one direction. However, both the larval body and central nervous system are symmetric on either side of the dorsal and ventral

midlines. The hemisegment unit is important to consider during rolling behavior, since the bilaterally symmetric neural and muscle activity that occurs during crawling must be broken during rolling, setting up a fundamental difference between these two behaviors.

In this study, we examine the muscle activity and motor circuits responsible for escape bending and rolling using a combination of high-speed 3D imaging of fluorescent calcium indicators expressed in muscles, functional manipulations of motor circuits, and connectomics approaches. We compare our findings to the motor activity that drives crawling to identify what features of peristaltic locomotor drive are preserved in escape, and what motor features are unique to escape locomotion. Both behaviors involve sequential motor activity and antagonistic drive of distinct muscle groups, but our results highlight fundamental differences in the motor patterns. In particular, muscle contractions progress circumferentially around the larva during rolling, in contrast to the anteroposterior progression of muscle contractions during crawling. These data provide a foundational view of motor activity during escape, narrowing in on a full sensory to motor understanding of an escape behavior.

Results

Muscle activity patterns in rolling escape

Drosophila larval escape is comprised of C-shaped bending followed by lateral rolling[22]. Rolling can be triggered experimentally by activation of nociceptive sensory neurons or by central neurons including the Goro command neuron[26]. We confirmed that in response to optogenetic activation of Goro or a global heat nociceptive stimulus, larvae engage in bending and rolling behavior. We found that larvae can bend to the left or right, and, independent of bend direction, may roll in a clockwise or counterclockwise direction (**Figure 1A; Video S1**). Thus, upon optogenetic activation of nociceptive circuitry, larvae can engage four distinct, yet related, escape motor patterns.

Escape circuitry is well-studied in *Drosophila* larvae, but how circuitry converges on premotor and motor systems is not known. We therefore sought to determine the muscle activity that underlies the escape rolling motor pattern. We imaged larvae using Swept Confocally-Aligned Planar Excitation (SCAPE) microscopy, a volumetric imaging technique that permits high-speed, high-resolution, 3D imaging of behaving animals[31–38]. We induced rolling using Goro activation in larvae expressing mCherry and GCaMP6f in all body wall muscles. We resolved activity of individual muscles along the entire length of the larva and approximately half of the body thickness, at 10 volumes per second (**Figure 1B**; **Figure S1A,B; Video S2)**. We predicted that as GCaMP6f/mCherry ratios increased, muscle length would decrease, reflecting

muscle contraction upon activation. Indeed, these two measurements showed an inverse relationship, suggesting that GCaMP6f/mCherry ratios can be used as an indicator of muscle contraction (**Figure S1C**). We focused on muscles in mid-segments A2-A4 since activity in these showed the greatest dynamic range (**Figure S1C**). We analyzed roughly 19 muscles per hemisegment in A2-A4 across multiple roll events, totaling over 370 muscle measurements.

SCAPE movies revealed that muscles are most active along the bent side of the larva, consistent with a role for asymmetric muscle contractions in C-shaped bending (**Video S3**; **Figure 1B**). Ratiometric calcium signals for many muscles tended to decrease as muscles moved out of the bend (**Video S3; Figure S2B-D**) and to increase as muscles rotated into the bend (**Video S3; Figure S2E**). To contrast escape rolling and crawling at the level of individual muscles, we compared SCAPE imaging data collected during rolling to previously acquired confocal data on muscle activity during crawling[21] (**Figure 1B,C**). As expected, measurements of muscle peak activity during crawling revealed a delay between muscle contraction in neighboring segments during peristalsis (**Figure 1C,D**). By contrast, during rolling, segmentally homologous muscles showed synchronous contractions, primarily on the side of the larva entering the bend. Also, in contrast to peristalsis, sequential muscle activity traveled around the circumference of the larva during rolling (**Figure 1 B,E,F, Figure S3**). Notably, we found that while dorsal (D) and ventral (V) longitudinal and oblique muscles demonstrated significantly greater activity along the bent side than the stretched side of the larva, lateral transverse (LTs) and ventral acute (VAs) muscles show roughly equivalent activity on bent and stretched sides on average (**Figure 2A-C**). Therefore, LT and VA muscles do not follow the typical circumferential wave of activity seen in other body wall muscles.

Altogether, these data demonstrate crucial distinctions between motor patterns during rolling and crawling: 1) muscle activity during rolling is synchronous across segments but is intersegmentally asynchronous during crawling; 2) muscle activity is left-right asymmetric during rolling but is left-right symmetric during crawling; 3) rolling involves progression of muscle contractions around the circumference of the larva, while crawling involves progression of muscle contractions along the anteroposterior axis. As an important exception to (2) above, we predict that as larvae roll, there are periods of L-R hemisegmental symmetry when homologous muscles along the dorsal and ventral midline enter the bend and co-contract. However, rolling and crawling are similar in that the within-segment muscle activity patterns both demonstrate opposing functions of longitudinally-spanning versus transverse-spanning (LT and VA) muscles.

Identifying candidate circuits for circumferential muscle contraction sequences

We next examined electron microscopic (EM) connectome data[22] to determine whether MN structure and PMN-MN connectivity could provide insights into the basis of bending and rolling. Activity measurements indicated two requirements for the escape motor pattern: 1) left-right asymmetric muscle contraction during bending, and 2) circumferential propagation of this contraction during rolling. To first gain insight into asymmetric muscle contraction, we focused on the spatial distribution of postsynaptic fields on MN dendrites. Previous studies showed that MNs innervating lateral muscles have ipsilateral dendritic arborizations while some MNs innervating midline muscles have both ipsi- and contralateral dendritic arborizations[21,39–41]. Consistent with this, we found that postsynaptic fields on MNs innervating the lateral muscles are located in the ipsilateral side only. Hence, there is no overlap between the fields of left and right MN counterparts (**Figure S4A,B)**. By contrast, the left and right MNs innervating the dorsal muscles show partial overlap in their postsynaptic fields (**Figure S4C)**. This partial overlap of fields could support the momentary bilateral symmetry that occurs as the dorsal midlines rotate into the bend. Such partial overlap is also seen for the left and right MNs innervating the ventral muscles (**Figure S4D,E)**, which could support the transient synchronous activity of left and right ventral muscles while passing through the bend side.

Next, we examined the PMN-MN connectome for circuits that could support circumferential propagation of contraction. First, we identified multiple PMNs that synapse onto MNs with spatially clustered target muscles in the periphery. Specifically, PMNs that synapse primarily to MNs innervating one spatial muscle group are more likely to synapse onto neighboring regions around the circumference of the larva, such as dorsolateral muscles (i.e., DLs, DOs, and LTs), ventrolateral muscles (i.e., VOs, VLs, and LTs) (**Figure 3A, Figure S5A**), and/or muscles flanking dorsal midline (i.e., left-right DLs) (**Figure 3B, Figure S5B**). To verify this phenomenon across all PMNs, we observed the cosine similarity between individual PMN projection patterns relative to downstream muscle drive and found that muscles more proximal along the circumference of the larva have higher overlap in PMN drive than those distal to each other (**Figure S5C**). On the other hand, MNs that innervate spatially distant muscles (i.e., lateral transverse muscles LTs on the left and right side) receive inputs from an exclusive set of PMNs (i.e., right PMNs synapsing with right LTs and vice versa) (**Figure 3C, Figure S5B**).

As a specific example for PMNs driving neighboring muscles, we found that two presumptive excitatory PMNs in the right hemisgment (A03a1_a1r and A03a3_a1r PMNs) are presynaptic to MNs innervating dorsolateral muscles (DLs and DOs) on the animal's right side, while they also make a smaller number of synapses with MNs innervating DL muscles on the left side (**Figure 3D**). Thus, activity of these right A03 PMNs should strongly activate the right

dorsolateral muscles and weakly activate the DL muscles on the left side. Then, activation of the left counterparts of these PMNs should have a mirror effect and strongly activate the left dorsolateral muscles while weakly activating the DL muscles on the right side. Sequential activation patterns of left and right A03 PMNs should therefore facilitate the circumferential progression of dorsolateral muscle contractions from right to left hemisegments, a pattern that is seen during clockwise rolling (**Figure 3E**). Further analysis of connectome data revealed that two inhibitory PMNs (A23a and A31k) have connectivity patterns similar to the excitatory A03a1 and A03a3 PMNs (**Figure 3D**). Such a synaptic organization raises the possibility that circumferential propagation of MN activity could be followed by circumferential inhibition of muscles. As A23a and A31k inhibit dorsolateral muscles, other excitatory PMNs may activate lateral and/or ventral muscles, thereby enforcing wave progression (**Figure 3E**).

To quantitatively test the significance of the observed circumferential structure of PMN-MN-Muscle connections, we compared the dorsoventral structure of PMN-MN outputs to that which would be expected by chance. Specifically, we performed a shuffling procedure that preserves the general statistics of PMN-MN connectivity while randomizing specific PMN-MN pairs (**Figure S5D,E**). We found that the dorsoventral structure of real PMN-MN-Muscle connectivity patterns of all PMNs combined, as well as only PMNs previously identified as excitatory or inhibitory, is significantly greater than expected by chance (**Figure S5F**). This supports the likelihood that multiple specific premotor motifs could aide in driving a circumferential wave of muscle contractions, like those detailed above, and with precisely timed handoff from excitatory to inhibitory PMNs (**Figure 3D**).

Taken together, the PMN-MN-Muscle connectome is structured in way that sequential firing of excitatory and then inhibitory PMNs in one side followed by the activation of their counterparts on the other side could underlie the progression of muscle contraction waves around the circumference of the larva. In **Figure 3E and F,** we propose a model describing how circumferential progression of muscle activity enables larvae to produce the four different patterns of rolling presented in this study. Notably, this model suggests that a counterclockwise roll involves clockwise progression of muscle contraction, and vice versa.

Tonic MNs innervating ventral and lateral muscles are essential for escape rolling

We next sought to understand how different MNs and muscles contribute to rolling. Our analysis of muscle activity indicated that longitudinally-spanning muscles and transversely-spanning muscles are activated in distinct phases during rolling (**Figure 2**), raising the possibility that coordination of the activity of these muscles groups is critical for rolling. To test

this possibility, and determine the roles of different muscle groups in rolling, we optogenetically activated Goro command neurons while chronically silencing subsets of MNs using Kir2.1. Many larval body muscles are co-innervated by type Is and a single type Ib excitatory MNs (**Figure 4A**). Each type Is MN innervates multiple target muscles, has a phasic firing pattern, and makes smaller synaptic boutons in neuromuscular junctions (NMJs), whereas type Ib MNs typically innervate one muscle, have a tonic firing pattern, and establish big synaptic boutons in their NMJs[42,43].We found that silencing the type Ib MNs innervating ventral longitudinal (VL) and dorsal oblique (DO) muscles blocked both bending and rolling (**Figure 4B**). These data are consistent with a key role for ventral longitudinal muscles in nociceptive escape. We found that silencing MNs that drive other groups of muscles had different impacts on rolling. Namely, larvae with silenced LT-innervating MNs could still bend but were unable to roll more than 90° (i.e., from their ventral to lateral side) (**Figure 4C,D Video S4**), highlighting a functional difference of LT muscle activity in rolling. Dorsal longitudinal (DL) muscles also contribute to rolling performance, but to a lesser extent than LT or VL muscles, since silencing DL-innervating MNs reduced rolling less profoundly than silencing other MN lines (**Figure 4B,C,D**). Selective silencing of the type Is MNs had little effect on rolling performance; however combinatorial silencing of type Is and different subsets of type Ib MNs led to a lower rate of rolling success than when either type Ib or type Is MNs were silenced alone (**Figure 4B,C,D**).

Taken together, we conclude that, while all different muscle types contribute to efficient rolling performance, the ventral and lateral muscles are the most crucial groups of muscles for initiation and execution of escape rolling. Furthermore, type Is input may act in synergy with type Ib inputs to generate robust rolling escape behavior.

Discussion

Escape is a fundamental form of locomotion and critical for the survival of all animals. To understand the neural mechanisms of an escape behavior, we have performed live imaging of muscle activity across animals as they perform escape, analyzed a connectome for motor circuits that could support the unique muscle propagation wave that coordinates this escape motor program, and performed MN silencing experiments to determine muscle groups whose activity is necessary for escape. This work has illuminated fundamental distinctions and similarities between motor patterns underlying forward crawling and escape in the larva, and starts to uncover the circuit basis for escape.

Enhancements of SCAPE microscopy to permit studies of rolling behavior

Our ability to identify patterns of muscle activity during rolling was aided by the further development of dual-color SCAPE. High-speed, high-resolution SCAPE microscopy has previously captured muscles in behaving larvae[44] and dual-color proprioceptor activity during crawling behavior[33]. Expanding dual-color SCAPE imaging here enabled ratiometric quantification of muscle activity and discrimination of activity signals from passive changes in fluorophore density within muscles. This imaging method also allowed measurement across muscles at different focal depths during freely moving behavior, including muscles within the C-shaped bend during escape. We expect that further development of SCAPE, for example wider field of view optics and simultaneous collection of signals from multiple angles, will allow coincident imaging in the CNS and muscles and test some of the hypotheses about PMN to MN transformations that underlie rolling, and a number of other behaviors, in simple model organisms.

Separable sequences of muscle activity during rolling

Animal movement universally involves coordinated sequential muscle activity. We find that the segmentally synchronous circumferential progression of muscle contractions define escape rolling behavior in *Drosophila* larvae. This sequence of activity progresses in a clockwise or counterclockwise manner, which determines the direction of rolling. A recent independent investigation of the motor pattern that generates larval escape similarly found that a circumferential wave of muscle activity occurs during rolling, and that the sequence of this wave determines the rotational direction of the larva[45]. Whether the circumferential sequence is the primary motor activity that promotes rolling, or whether other independent patterns are involved, is so far unclear. However, our muscle imaging revealed evidence that, during rolling, LT muscles contract as part of a separate, out-of-phase sequence relative to the major wave of activity of longitudinal muscles. LT muscles begin to contract after D and V longitudinal muscles also during crawling, suggesting special roles for these muscles in both forms of locomotion. During forward crawling, contraction of LT muscles shortens the dorsoventral axis, providing a force that is thought to push the neighboring internal organs to the anterior side[20]. We speculate that during rolling LT muscle activity provides a circumferential pulling force that is essential for body rotation. Interestingly, while silencing the LT innervating MNs substantially compromises rolling behavior, it has no effect on forward crawling[28].

One crucial future goal will be to understand how segmentally synchronous contractions of specific groups of muscles are initiated and then how contraction propagates to other muscle

groups in a precise circumferential sequence during rolling. The fundamental distinctions between bodily coordination during escape versus crawling illustrate the remarkable propensity for even relatively simple nervous systems to generate vastly different circuit dynamics based on context. Prior to this work, it was unknown whether escape rolling would involve a peristaltic wave component, like that observed in crawling, and our work has demonstrated the absence of a peristaltic wave during rolling. Understanding at a circuit level how the larval motor system switches between these two global patterns of activity remains an open question. Despite these global differences, the analogies in LT activity in muscle contraction sequences during crawling and rolling raise the question of how translatable our knowledge of premotor crawling circuits will be for understanding rolling. It will be especially important to determine whether excitatory and inhibitory microcircuit motifs that coordinate crawling[43] also coordinate rolling muscle contractions. Further, understanding how the larva transitions between peristaltic and escape locomotor modes remains an open question.

Insights into motor circuits critical for rolling behavior

Our functional manipulations of MNs innervating distinct muscle subgroups highlight the modularity of motor control in larval escape. Larvae can exclusively bend, or perform bending and rolling. These behavioral components occur probabilistically and are dependent on the precise nature of sensory input to the larva[24,26,27]. Some sensory interneurons are necessary and sufficient for escape bending to occur but are not necessary for escape rolling[27]. Namely, we see that a circumferential wave of bend-promoting contractions occurs in longitudinal muscles, while counteracting contractions occur in transverse muscles that could provide a pulling force. Our MN silencing experiments demonstrate that longitudinally-spanning muscles are essential for larval bending and rolling altogether, while transverse muscles are only essential for rolling. These findings are congruent with previous work demonstrating that neurons driving transverse muscles are essential for body rotation in self-righting[46] and rolling[28]. Uncovering the premotor circuit modules that drive the bend and the roll could provide insight into how the larval nervous system generates many motor components of its behavioral repertoire.

The relative roles of Is and Ib MNs in different larval behaviors is still debated[42,47–49]. Our MN silencing experiments showed that silencing type Ib MNs innervating ventral or lateral muscles led to substantial defects in rolling behavior, whereas silencing broadly-projecting type Is MNs minimally impacted rolling unless in combination with type Ib MN silencing. Phasic Is MNs have a higher probability of vesicle release at the NMJ, demonstrate elevated presynaptic

calcium influxes upon stimulation, and contain larger synaptic vesicles per synapse than tonic Ib MNs, leading to higher amplitude EPSPs in muscles following type Is activity[47,50,51]. For these reasons, Ib and Is MNs are sometimes called “weak” and “strong” MNs, respectively[47,50]. On the other hand, type Ib NMJs have higher levels of readily-releasable vesicle pool, a higher number of active release sites than Is boutons, and are recruited earlier and for a longer duration during larval movement[47–50]. These physiological properties of type Ib tonic and type Is phasic MNs are determined by their distinct transcriptional profiles[51], and permit a division of labor during muscle contraction, where type Ib activity can coordinate specific, finer muscle contraction timing with varying levels of contractile force upon low-level premotor input, while type Is activity is recruited at high-level premotor input to increase contractile force of ongoing behavior or make large, forceful shifts in movement[47–50]. In conjunction with our results, these properties suggest that type Ib MNs are crucial for driving the main muscle contraction pattern underlying rolling, while type Is MNs merely contribute additional contractile force to escape, consistent with the minimal impact of type Is MN silencing on crawling behavior[48]. These findings are also consistent with tonic and phasic motor control principles observed in mammalian systems[52–54], adult *Drosophila* walking[55] and flight[56], and other escape motor circuits[18].

We uncovered MN post-synapse distributions and patterns of PMN-MN connectivity that could support propagation of muscle contractions around the circumference of the larva during rolling behavior. Studies of PMNs that innervate midline muscles could reveal how the circumferential wave progresses from left to right sides of the larva’s body. Specifically, PMNs that demonstrate bilateral drive to midline muscles essential for bending and rolling could be necessary for action selection and maintenance of specific escape rolling directions by permitting the circumferential sequence across left and right boundaries of the body. Bridging the gap between Goro escape-promoting command neurons to specific excitatory and inhibitory PMNs through further connectome reconstruction and circuit manipulation is a crucial next step in understanding the basis of larval escape. Continued pursuit of the sensorimotor circuits that drive escape in the larva will more broadly uncover the circuit mechanisms responsible for transforming sensory information into robust and flexible behaviors across taxa.

Materials and Methods:

Key Resources Table

Reagent type (species) or resource	Designation	Source or reference	Identifiers	Additional information
Genetic reagent (*Drosophila melanogaster*)	w1118	BDSC		Global heat + vibration assay line, crossed as control for MN silencing experiments
Genetic reagent (*Drosophila melanogaster*)	R69F06-Gal4	BDSC	# 39497	Goro line
Genetic reagent (*Drosophila melanogaster*)	44H10-LexA, Aop-GCaMP6f; Aop-mcherry, UAS-Chrimson-mcherry	Aref Zarin		Optogenetics line
Genetic reagent (*Drosophila melanogaster*)	44H10-LexA, Aop-mcherry; 44H10::GCaMP6f,UAS-Chrimson-mcherry	Aref Zarin		SCAPE ratiometric muscle imaging
Genetic reagent (*Drosophila melanogaster*)	69E06-LexA; Aop-Chrimson-mCherry, UAS-Kir2.1-eGFP	Aref Zarin		Goro activation and MN silencing
Genetic reagent (*Drosophila melanogaster*)	27E09-Gal4	BDSC		MN silencing
Genetic reagent (*Drosophila melanogaster*)	RRa-Gal4	Albert Cardona		MN silencing
Genetic reagent (*Drosophila melanogaster*)	BarH1-Gal4 (w[*]P{w[+mW.hs]=GawB}NP4099 / FM7c)	Kyoto Stock Center	DGRC# 104-601	MN silencing
Genetic reagent (*Drosophila melanogaster*)	CQ-Gal4	Miki Fujoka, Jim Jaynes		MN silencing

Contact for Reagent and Resource Sharing:

Further information and requests for resources should be directed to and will be fulfilled by the Lead Contact, Aref Zarin (azarin@bio.tamu.edu).

Experimental Model and Subject Details:

Drosophila melanogaster strains were reared on standard molasses food (agar, cornmeal, yeast, molasses, methylparaben, ethanol, propionic acid, penicillin, streptomycin) at 25°C, 60% humidity. Animals of either sex were used. For behavior experiments, third instar larvae were used. For muscle imaging experiments, late first and early second instar larvae were used.

Method Details:

Behavior Experiments:

For behavior experiments, at least two sessions, performed on separate days, were performed for each genotype. Larvae were only tested once. Sample sizes for global heat + vibration and optogenetic Goro activation escape assays were designed to replicate recently published larval escape assay data[26]. Escape pattern frequency and initial kinematic characterization experiments were conducted using the FIM (Frustrated total internal reflection Imaging Method)[59]. Videos were acquired at 50 frames per second with a Basler ACE acA2040-90uc four megapixel near infrared sensitivity enhanced camera equipped with CMOSIS CMV4000 CMOS sensor. Camera was equipped with LM16HC-SW lens (Kowa), and BN880-35.5 filter (Visionlighttech). IR diodes (875 nm, Conrad) were used for FTIR imaging and images were acquired using Pylon camera software (Basler). Animals were placed on 0.8% agar surface ~2 mm thick (Molecular grade, Fisher Scientific).

For the global heat and vibration assay, we developed a novel implementation of FIM, where the agar surface was uniformly heated and temperature was read out using a Elitech STC-1000 and two 10 kOhm temperature probes. These probes measured temperature in the FIM table chamber, which was heated by four LUBAN Mini Hot Air Guns, and the agar substrate itself. Third instar w1118 larvae were rinsed and transferred to a petri dish with 0.8% agar at least 10 minutes prior to experimentation. Then, larvae were gently transferred with a paintbrush to the agar surface. Vibration was generated using Logitech Multimedia Speakers Z200 with Stereo Sound for Multiple Devices. The composite 1000Hz and wasp sound, played at 100dB, was previously published in Wreden *et al.*, 2017[60]. Behavior was recorded immediately.

For optogenetic Goro activation experiments, larvae were raised in the dark on molasses food with 1 mM all-*trans*-retinal (ATR). These larvae were offspring of 44H10-LexA, Aop-GCaMP6f; Aop-mcherry, UAS-Chrimson-mcherry female and R69F06-Gal4 male flies. Larval care prior to experimentation was the same as in the global heat assay, above. Two rings of Blue (470 nm) LED lights (WFLS-G30 × 3 WHT, SuperBright LEDs) of 5 inches and 8 inches diameter were placed approximately 5 inches underneath the FIM table. LED brightness was programmed for experiments using custom code in ARDUINO, as the LEDs' pulse width modulation was controlled by an ARDUINO Mega 2560 board. For Goro activation experiments, blue LEDs were active at 2230 uW/mm^2. Larvae that failed to move at all during trials were excluded from any analysis. Bend and roll pattern frequencies were quantified manually by evaluating TIFF stacks in FIJI (https://imagej.net/Fiji).

To assess the roles of different MNs on escape, we performed functional silencing of MN-Gal4 lines. Rolling was induced and imaged in larvae carrying the LexA driver for Goro neurons and Chrimson. Constitutive silencing of MNs was achieved via the expression of the inward-rectifying potassium channel, Kir. 69E06-LexA; Aop-Chrimson-mCherry, UAS-Kir2.1-eGFP females with MN-Gal4 males were crossed for experimental groups, and 69E06-LexA; Aop-Chrimson-mCherry, UAS-Kir2.1-eGFP males with w1118 females were crossed for control groups. For the experimental and control groups involving CQ-Gal4 and BH1-Gal4, L1 larvae were used due to early lethality and reduced transgene expression in later instars, respectively. For other crosses, L3 larvae of the experimental and control groups were used. Kir2.1 lethality when crossed to BH1-Gal4 or decreased expression of CQ-Gal4 in L3 animals. Larvae were raised on molasses food in dark and fed with 1mM all-trans-retinal (ATR) 24 h prior to the experiment. Larvae were picked from food, rinsed, and given a 30-second rest before imaging to avoid any effect of the minimum light exposure during the process. The animals were then placed onto a 1.5% agarose pad in a 10cm round Petri dish and imaged with an iPhone SE (second generation, Apple Inc.) camera at 30fps. For L1 animals, the larvae and agarose gel were placed under a Stemi 508 dissection scope (Zeiss) and imaged by the iPhone SE camera through a microscope phone adapter (Gosky) with 16X built-in eyepiece (the original 10X eyepiece was removed from the dissection scope). Optogenetic activation of rolling was induced with 30 seconds of intense, uniformly applied white light from beneath the agarose gel (Oeegoo 18W square LED ceiling light) after a 10-second dark period.

Rolling performance was scored manually after blinding data. Rolling success was defined as a larva completing at least one 360° roll (after body bending, able to rotate in a single direction from dorsal side up to dorsal side up). Video processing was done with freeware

FFmpegtool (https://ffmpeg.org/) and ImageJ (https://imagej.net/, National Institutes of Health, Bethesda, Maryland).

Confocal Image Acquisition:

Muscle activity during crawling was initially measured in Zarin *et al.*, 2019[21]. Briefly, images were acquired using a 10x objective on an upright Zeiss LSM800 microscope. GCaMP6f and mCherry fluorescence values were extracted from a previously acquired forward crawling video and ratiometric values from muscle ROIs (see SCAPE analysis) were subsequently compared to ratiometric muscle ROI values from SCAPE escape images.

SCAPE Image Acquisition:

A custom-built Swept Confocally Aligned Planar Excitation (SCAPE) microscope, extended from that described in Voleti *et al.*, 2019[35] & Vaadia *et al.*, 2019[33], was used to acquire high-speed volumetric imaging of rolling larvae. The system utilizes a custom-made water chamber between the second and third objective lens to accommodate higher collection efficiency over a large field of view with 1.0 NA water immersion objectives throughout. 488nm and 561nm lasers were used to excite GCaMP and mCherry simultaneously, while also activating Chrimson for optogenetics. An image splitter with 561nm long pass dichroic mirror was used with 525/50 and 618/50 filters to split the image into two sCMOS cameras (Andor Zyla 4.2 plus) which enables acquisition of both green and red channels simultaneously with a field of view larger than 1.1mm in the lateral dimension. A 3D field of view with the size of the agar arena was acquired at 10 volumes per second to minimize the motion blur from the larva rolling behavior.

Larvae were raised and fed ATR for optogenetic activation as mentioned above. Larvae were imaged while in a thin 2% agarose chamber filled with distilled water. Each larva was assessed for brightness of muscle fluorophore expression and likelihood of rolling through epifluorescent screening, and the best overall larvae were placed into agar chambers using a fine paint brush. Each chamber was made using 3D-printed molds of different dimensions for late L1 and early L2 larvae of slightly different sizes.

SCAPE Image Processing & Analysis:

SCAPE volumetric data are inherently three-dimensional. To overcome 3D-segmentation difficulties but keep the richness of volumetric muscle data, we developed a custom MATLAB script to generate a 3D-averaged projection of all SCAPE data. Our 3D-

averaging method generates separate GCaMP and mCherry 2D images dynamically based on fluorescence histograms of the z-depth at each x,y pixel location, allowing us to isolate and average signal exclusively from muscle tissue. 3D-averaged projection images were then analyzed using modified versions of the custom MATLAB script from Zarin *et al.*, 2019 and a custom MATLAB script for measuring ratiometric signal and muscle length rapidly using interactive linearly interpolated linescans. For ratiometric signal vs. length measurements, lines were drawn on select frames for example muscles segments A1-A6 on two rolling SCAPE ratiometric movies, and linear interpolations of linescans on intermediate frames were checked frame-by-frame for each movie. Ratio values and muscle lengths were quantified using custom MATLAB scripts. For ROI-based rolling muscle activity analysis, ROIs were drawn manually on non-overlapping portions of each muscle for each segment from A2-A4 on a frame-by-frame basis. Because puncta were present throughout muscles in the mCherry images, pixels with a fluorescence value greater than 90% of the distribution of fluorescence values within the mCherry ROI were discarded in both the mCherry and GCaMP channels to prevent biased ratiometric signal. The ratio of fluorescence between the ROI pixels of the mean depth-projected GCaMP image and the mean-depth projected mCherry image was calculated. The mean of this ratiometric value was extracted for each time point of the ROI, generating individual muscle activity traces. Four roll bouts (one complete revolution based on muscle locations) from four larvae were selected for rolling muscle activity analysis. Subsequent analyses were performed using custom MATLAB scripts.

For comparisons between ratiometric muscle activity values of crawling and rolling, normalized time at maximum ratiometric values were extracted. Statistical analyses were performed as described below. For bend vs. stretch side comparisons of individual muscle activity during rolling, ROI centroids were tracked and, according to the bend and rotation directions of the larvae, divided into four quartiles based on spatial position within the larva's body at each time point. Ratiometric values from the most bent quartile and ratiometric values from the most stretched quartile were extracted and averaged for each muscle. These values were then compiled, z-scored, and averaged across segments and across three roll videos, providing a "bend" and "stretch" ratiometric values for each muscle, shown in the boxplots in **Figure 2A**. Statistical analyses were performed using custom programs written in MATLAB. For muscle activity peak differences, Wilcoxon Rank Sum tests were used.

Electron microscopy, CATMAID reconstructions, and Quantitative Analysis:

PMN-MN connectome previously reconstructed in Zarin *et al.*, 2019[21] were used to generate **Figure 3, Figure S4, and Figure S5.** For quantitative analysis of the dorsoventral structure of PMN-MN connectivity, each MN was assigned a spatial position 1-30 to reflect how their projections map onto the dorsoventral axis of muscles in the body wall. For example, DL muscles 1, 9, 2 and 10 were assigned position numbers 1, 2, 3, and 4, respectively; while VO muscles 28, 15, 16, and 17 were assigned position numbers 27, 28, 29, and 30, respectively. A weighted average was calculated for each PMN using this MN position assignment. PMNs were then sorted by their strength of connectivity to dorsoventrally organized MNs, and averaged left and right PMN-MN weights were z-scored and displayed (**Figure S5A**). Following this sorting of PMNs based on their spatial connectivity strengths, the connection weights of PMNs to MNs were binarized (**Figure S5D**). Cosine similarity analysis was then performed between each PMN, providing a metric of similarity, or more literally, distance between the pairwise binary vectors of each PMN's spatially organized outputs. A cosine similarity of 1 means pairwise PMN-MN connectivity vectors overlap perfectly, or have identical outputs, while a cosine similarity of 0 means pairwise PMN-MN connectivity vectors are orthogonal, or have no common outputs (**Figure S5C**).

To determine whether global PMN-MN connectivity patterns demonstrate greater dorsoventral patterning with respect to downstream muscles than expected by chance, a shuffling procedure was employed, similar to that used in Hayashi *et al.*, 2022[61]. Specifically, to generate a statistically meaningful null hypothesis of how PMN-MN connectivity could be structured, binary weights from each PMN onto all MNs were randomly selected with the number of outputs that each PMN makes and the probability of inputs to each MN constrained by the properties of the real PMN-MN connectivity matrix. This constrained global statistics of the 1000 shuffled connectivity matrices to match the statistical properties of the real connectivity matrix without constraining specific PMN-MN partner identities (**Figure S5E**). The relative dorsoventral structure of real PMN-MN connectivity compared to null connectivity was assessed by performing linear regression on the weighted averages of real vs. shuffled PMN outputs and comparing the regression coefficients between real and shuffled data (**Figure S5F**). The regression coefficients serve as a metric of how strongly PMNs prefer MNs based on muscle dorsoventral order, and the regression coefficients for real connectivity data lie outside the 95% confidence interval of the null distribution of regression slopes, demonstrating statistical significance. Unilateral vs. bilateral PMN-MN projection comparisons according to spatial muscle groups were performed by calculating the weighted average of bilateral vs. unilateral inputs onto MNs, and statistical difference between pairs was determined using the Mann-Whitney U test (**Figure S5B)**.

Data and Software Availability:

Behavioral analysis, 3D averaging, signal extraction, and subsequent muscle activity analysis were performed using custom MATLAB scripts that have been included with manuscript submission and are also available here: https://github.com/cooneypc4/larval_escape_manuscript. The source data that support the findings of this study are available from the corresponding authors upon request.

Acknowledgements

We thank Ashok Litwin-Kumar for providing guidance on quantitative analysis of connectome data. We thank Albert Cardona, Richard D. Fetter, and the HHMI Janelia Fly EM Project Team for providing the raw data of the whole CNS EM volume. We thank Akira Fushiki and Maarten Zwart for annotating neurons, and Keiko Hirono for generating transgenic constructs. We thank Grace Shin for assisting with behavioral assay development. We thank Malte Casper for supporting SCAPE data processing. Stocks obtained from the Bloomington Drosophila Stock Center (NIH P40OD018537) were used in this study. Research reported in this publication was supported by an institutional startup fund from Texas A&M University (AAZ), NIH NINDS R01NS061908 (W.B.G), NIH BRAIN 5U01NS094296 and 1UF1NS108213 (E.M.C.H. and W.B.G.), DoD, MURI W911NF-12-1-0594, and Simons Foundation Collaboration on the Global Brain (E.M.C.H.), and an NSF predoctoral fellowship DGE 2036197 (PCC). The content is solely the responsibility of the authors and does not necessarily represent the official views of the National Institutes of Health.

References

1. Arendt, D., Tosches, M. A. & Marlow, H. From nerve net to nerve ring, nerve cord and brain-evolution of the nervous system. *Nat Rev Neurosci* **17**, 61–72 (2016).
2. Branco, T. & Redgrave, P. The Neural Basis of Escape Behavior in Vertebrates. *Annu Rev Neurosci* **43**, 417–439 (2020).
3. Card, G. M. Escape behaviors in insects. *Current Opinion in Neurobiology* vol. 22 180–186 Preprint at https://doi.org/10.1016/j.conb.2011.12.009 (2012).
4. Dickinson, M. & Moss, C. F. Neuroethology. *Curr Opin Neurobiol* **22**, 177–179 (2012).
5. Domenici, P., Blagburn, J. M. & Bacon, J. P. Animal escapology I: Theoretical issues and emerging trends in escape trajectories. *Journal of Experimental Biology* **214**, 2463–2473 (2011).
6. Domenici, P., Blagburn, J. M. & Bacon, J. P. Animal escapology II: Escape trajectory case studies. *Journal of Experimental Biology* **214**, 2474–2494 (2011).
7. Broekmans, O. D., Rodgers, J. B., Ryu, W. S. & Stephens, G. J. Resolving coiled shapes reveals new reorientation behaviors in C. elegans. *Elife* **5**, 1–17 (2016).
8. Edwards et al., 1999 - Fifty years of a command neuron- the neurobiology of escape behavior in the crayfish.
9. Eaton, R. C., Lee, R. K. K. & Foreman, M. B. The Mauthner cell and other identified neurons of the brainstem escape network of fish. *Prog Neurobiol* **63**, 467–485 (2001).
10. Huang, T.-C., Huang, Y.-J. & Lin, W.-C. Real-time horse gait synthesis. *Comput Animat Virtual Worlds* **24**, 87–95 (2013).
11. Kiehn, O. Decoding the organization of spinal circuits that control locomotion. *Nat Rev Neurosci* **17**, 224–238 (2016).
12. Fotowat, H., Harrison, R. R. & Gabbiani, F. Multiplexing of Motor Information in the Discharge of a Collision Detecting Neuron during Escape Behaviors. *Neuron* **69**, 147–158 (2011).
13. Hemmi, J. M. & Tomsic, D. The neuroethology of escape in crabs: From sensory ecology to neurons and back. *Curr Opin Neurobiol* **22**, 194–200 (2012).
14. von Reyn, C. R. *et al.* Feature Integration Drives Probabilistic Behavior in the Drosophila Escape Response. *Neuron* **94**, 1190-1204.e6 (2017).
15. Ache, J. M. *et al.* Neural Basis for Looming Size and Velocity Encoding in the Drosophila Giant Fiber Escape Pathway. *Current Biology* **29**, 1073-1081.e4 (2019).
16. Dunn, T. W. *et al.* Neural Circuits Underlying Visually Evoked Escapes in Larval Zebrafish. *Neuron* **89**, 613–628 (2016).
17. Donnelly, J. L. *et al.* Monoaminergic Orchestration of Motor Programs in a Complex C. elegans Behavior. *PLoS Biol* **11**, (2013).
18. Kennedy, D. & Takeda, K. Reflex control of abdominal flexor muscles in the crayfish. *J. Exp. Biol.* **43**, 221–227 (1965).
19. Bate, M. The embryonic development of larval muscles in Drosophila. *Development* **110**, 791–804 (1990).
20. Heckscher, E. S., Lockery, S. R. & Doe, C. Q. Characterization of Drosophila Larval Crawling at the Level of Organism, Segment, and Somatic Body Wall Musculature. *Journal of Neuroscience* **32**, 12460–12471 (2012).

634 21. Zarin, A. A., Mark, B., Cardona, A., Litwin-Kumar, A. & Doe, C. Q. A multilayer circuit
635 architecture for the generation of distinct locomotor behaviors in Drosophila. *Elife* **8**, 1–
636 34 (2019).
637 22. Tracey Jr., W. D., Benzer, S., Wilson, R. I. & Laurent, G. painless, a Drosophila gene
638 essential for nociception. *Cell* **113**, 261–273 (2003).
639 23. Hwang, R. Y. *et al.* Nociceptive Neurons Protect Drosophila Larvae from Parasitoid
640 Wasps. *Current Biology* **17**, 2105–2116 (2007).
641 24. Robertson, J. L., Tsubouchi, A. & Tracey, W. D. Larval Defense against Attack from
642 Parasitoid Wasps Requires Nociceptive Neurons. *PLoS One* **8**, (2013).
643 25. Grueber, W. B., Jan, L. Y. & Jan, Y. N. Dendritic tiling in Drosophila. *Development* **129**,
644 2867–2878 (2002).
645 26. Ohyama, T. *et al.* A multilevel multimodal circuit enhances action selection in Drosophila.
646 *Nature* **520**, 633–639 (2015).
647 27. Burgos, A. *et al.* Nociceptive interneurons control modular motor pathways to promote
648 escape behavior in Drosophila. *Elife* **7**, (2018).
649 28. Yoshino, J., Morikawa, R. K., Hasegawa, E. & Emoto, K. Neural Circuitry that Evokes
650 Escape Behavior upon Activation of Nociceptive Sensory Neurons in Drosophila Larvae.
651 *Current Biology* **27**, 2499-2504.e3 (2017).
652 29. Hu, C. *et al.* Sensory integration and neuromodulatory feedback facilitate Drosophila
653 mechanonociceptive behavior. *Nat Neurosci* **20**, 1085–1095 (2017).
654 30. Takagi, S. *et al.* Divergent Connectivity of Homologous Command-like Neurons Mediates
655 Segment-Specific Touch Responses in Drosophila. *Neuron* **96**, 1373-1387.e6 (2017).
656 31. Bouchard, M. B. *et al.* Swept confocally-aligned planar excitation (SCAPE) microscopy for
657 high-speed volumetric imaging of behaving organisms. *Nat Photonics* **9**, 113–119 (2015).
658 32. Hillman, E. M. *et al.* High-speed 3D imaging of cellular activity in the brain using axially-
659 extended beams and light sheets. *Curr Opin Neurobiol* **50**, 190–200 (2018).
660 33. Vaadia, R. D. *et al.* Characterization of Proprioceptive System Dynamics in Behaving
661 Drosophila Larvae Using High-Speed Volumetric Microscopy. *Current Biology* **29**, 935-
662 944.e4 (2019).
663 34. Hillman, Elizabeth M.C.; Voleti, Venkatakaushik; Li, Wenze; Yu, H. Light-Sheet Microscopy
664 in Neuroscience. *Annu Rev Neuroscie* **42**, 295–313 (2019).
665 35. Voleti, V. *et al.* Real-time volumetric microscopy of in vivo dynamics and large-scale
666 samples with SCAPE 2.0. *Nat Methods* **16**, 1054–1062 (2019).
667 36. Xu, L. *et al.* Widespread receptor-driven modulation in peripheral olfactory coding.
668 *Science (1979)* **368**, (2020).
669 37. Schaffer, E. S. *et al.* Flygenvectors: The spatial and temporal structure of neural activity
670 across the fly brain. *bioRxiv* 2021.09.25.461804 (2021).
671 38. Benezra, Sam E.; Patel, Kripa; Campos, Citlali; Hillman, E.M.C.; Bruno, R. Learning
672 enhances behaviorally relevant representations in apical dendrites. *bioRxiv* (2021)
673 doi:10.1101/2021.11.10.468144;
674 39. Mauss, A., Tripodi, M., Evers, J. F. & Landgraf, M. Midline signalling systems direct the
675 formation of a neural map by dendritic targeting in the Drosophila motor system. *PLoS*
676 *Biol* **7**, (2009).

40. Landgraf, M., Bossing, T., Technau, G. M. & Bate, M. The Origin, Location, and Projections of the Embryonic Abdominal Motorneurons of Drosophila . *The Journal of Neuroscience* **17**, 9642–9655 (1997).
41. Landgraf, M., Jeffrey, V., Fujioka, M., Jaynes, J. B. & Bate, M. Embryonic origins of a motor system: Motor dendrites form a myotopic map in Drosophila. *PLoS Biol* **1**, (2003).
42. Peron, S., Zordan, M. A., Magnabosco, A., Reggiani, C. & Megighian, A. From action potential to contraction: Neural control and excitation-contraction coupling in larval muscles of Drosophila. *Comparative Biochemistry and Physiology - A Molecular and Integrative Physiology* vol. 154 173–183 Preprint at https://doi.org/10.1016/j.cbpa.2009.04.626 (2009).
43. Clark, M. Q., Zarin, A. A., Carreira-Rosario, A. & Doe, C. Q. Neural circuits driving larval locomotion in Drosophila. *Neural Development* vol. 13 Preprint at https://doi.org/10.1186/s13064-018-0103-z (2018).
44. Bouchard, M. B. *et al.* Swept confocally-aligned planar excitation (SCAPE) microscopy for high-speed volumetric imaging of behaving organisms. *Nat Photonics* **9**, 113–119 (2015).
45. He, L., Borjon, L. & Daniel Tracey Jr, W. The motor pattern of rolling escape locomotion in Drosophila larvae. doi:10.1101/2022.11.03.514605.
46. Picao-Osorio, J., Johnston, J., Landgraf, M., Berni, J. & Alonso, C. R. MicroRNA-encoded behavior in *Drosophila*. *Science (1979)* **350**, 815–820 (2015).
47. He, K. *et al.* Physiologic and nanoscale distinctions define glutamatergic synapses in tonic vs phasic 1 neurons 2 3. *bioRXiV* (2022) doi:10.1101/2022.12.21.521505.
48. Newman, Z. L. *et al.* Input-Specific Plasticity and Homeostasis at the Drosophila Larval Neuromuscular Junction. *Neuron* **93**, 1388-1404.e10 (2017).
49. Schaefer, J. E., Worrell, J. W. & Levine, R. B. Role of intrinsic properties in Drosophila motoneuron recruitment during fictive crawling. *J Neurophysiol* **104**, 1257–1266 (2010).
50. Han, Y. *et al.* Botulinum neurotoxin accurately separates tonic vs. phasic transmission and reveals heterosynaptic plasticity rules in Drosophila. *Elife* **11**, (2022).
51. Jetti, S. K. *et al.* Molecular Logic of Synaptic Diversity Between Drosophila Tonic and Phasic Motoneurons Running Title: Molecular Diversity of Tonic and Phasic Neurons. doi:10.1101/2023.01.17.524447.
52. Henneman, E. Relation between Size of Neurons and Their Susceptibility to Discharge. *Science (1979)* **126**, 1345–1346 (1957).
53. Henneman, E., Somjen, G. & Carpenter, D. FUNCTIONAL SIGNIFICANCE OF CELL SIZE IN SPINAL MOTONEURONS. *Journal of Neurophysiology* **28**, 560–580 (1964).
54. Henneman, E., Somjen, G. & David, A. *EXCITABILITY AND INHIBITIBILITY OF MOTONEURONS OF DIFFERENT SIZES*. (1965).
55. Azevedo, A. W. *et al.* A size principle for recruitment of drosophila leg motor neurons. *Elife* **9**, 1–36 (2020).
56. Lindsay, T., Sustar, A. & Dickinson, M. The Function and Organization of the Motor System Controlling Flight Maneuvers in Flies. *Current Biology* **27**, 345–358 (2017).
57. Zwart, M. F. *et al.* Selective Inhibition Mediates the Sequential Recruitment of Motor Pools. *Neuron* **91**, 615–628 (2016).
58. Kohsaka, H. *et al.* Regulation of forward and backward locomotion through intersegmental feedback circuits in Drosophila larvae. *Nat Commun* **10**, 1–11 (2019).

59. Risse, B. *et al.* FIM, a Novel FTIR-Based Imaging Method for High Throughput Locomotion Analysis. *PLoS One* **8**, (2013).
60. Wreden, C. C. *et al.* Temporal Cohorts of Lineage-Related Neurons Perform Analogous Functions in Distinct Sensorimotor Circuits. *Current Biology* **27**, 1521-1528.e4 (2017).
61. Hayashi, T. T. *et al.* Mushroom body input connections form independently of sensory activity in Drosophila melanogaster. *Current Biology* **32**, 4000-4012.e5 (2022).

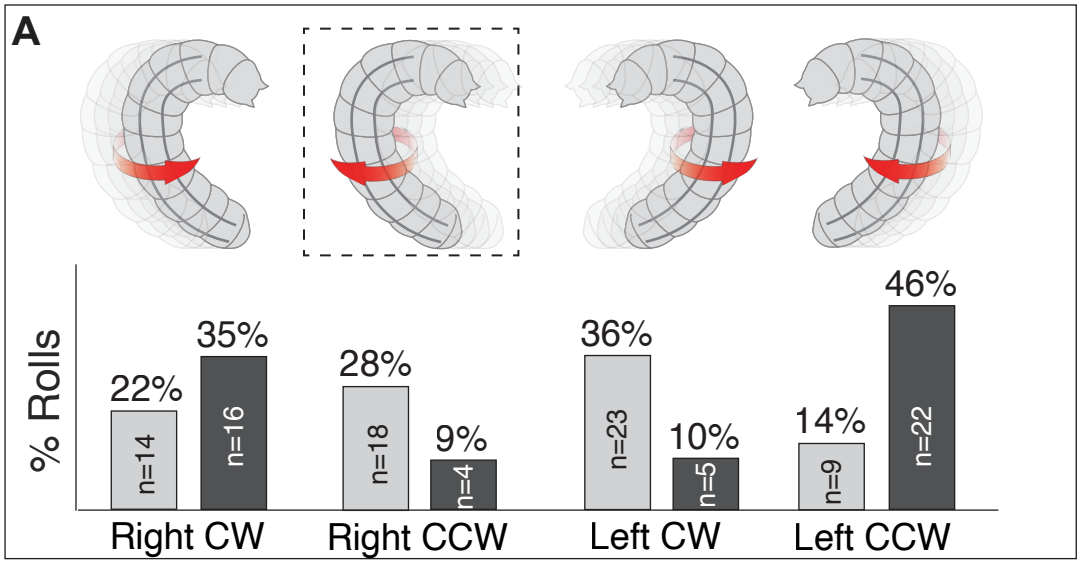
A
% Rolls
22%
35%
28%
9%
36%
10%
14%
46%
n=14
n=16
n=18
n=4
n=23
n=5
n=9
n=22
Right CW
Right CCW
Left CW
Left CCW

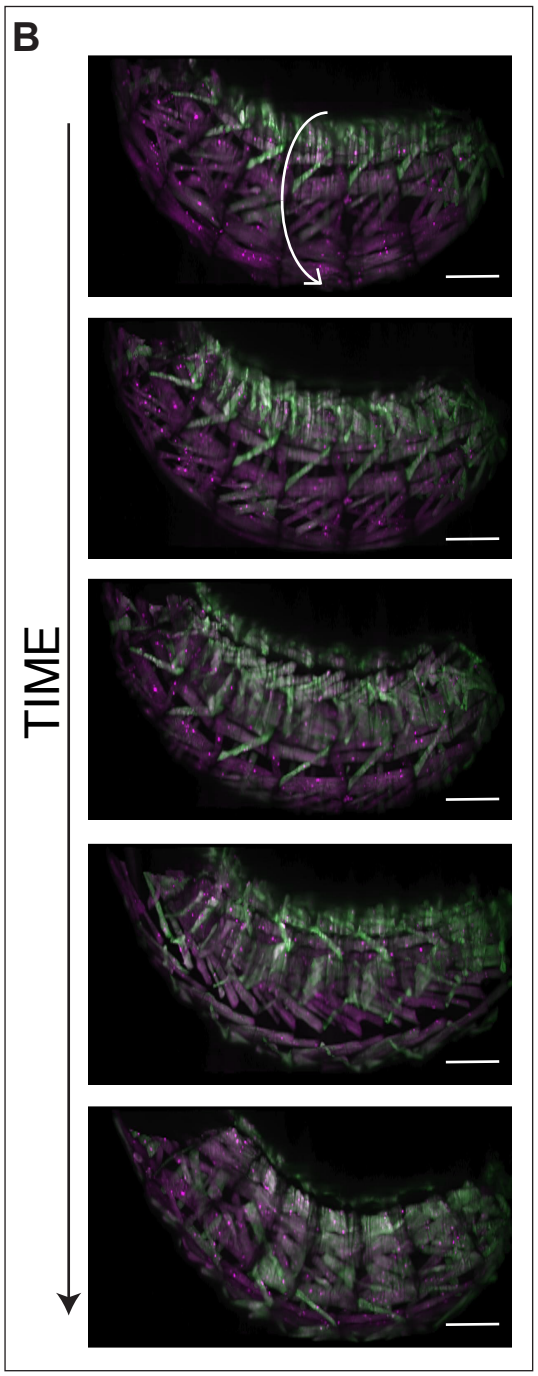
B
TIME

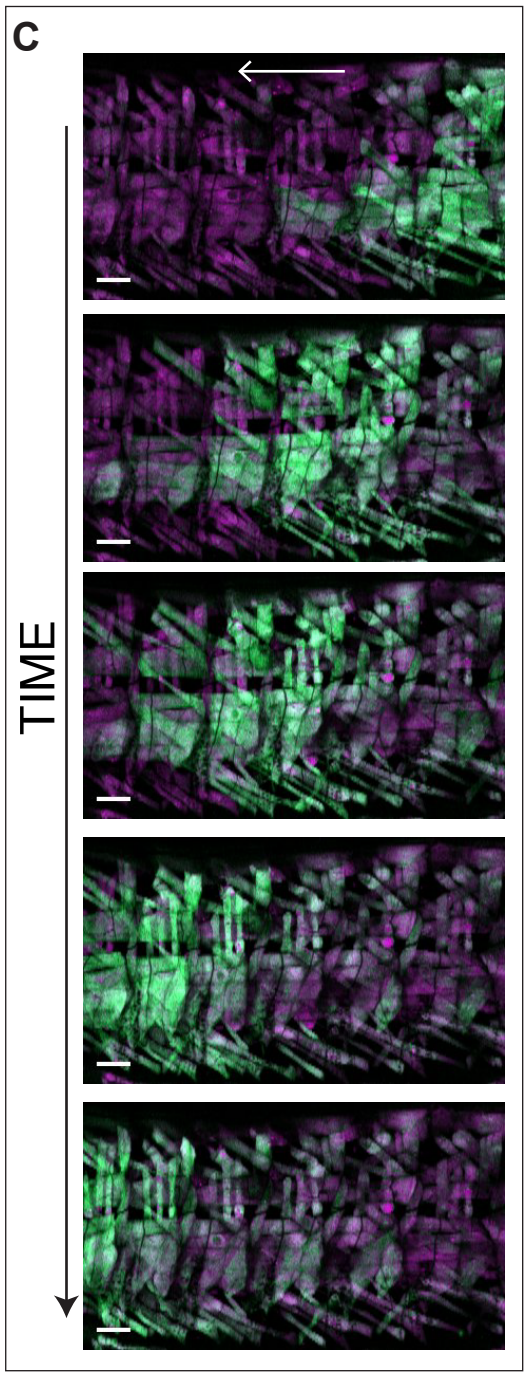
C
TIME

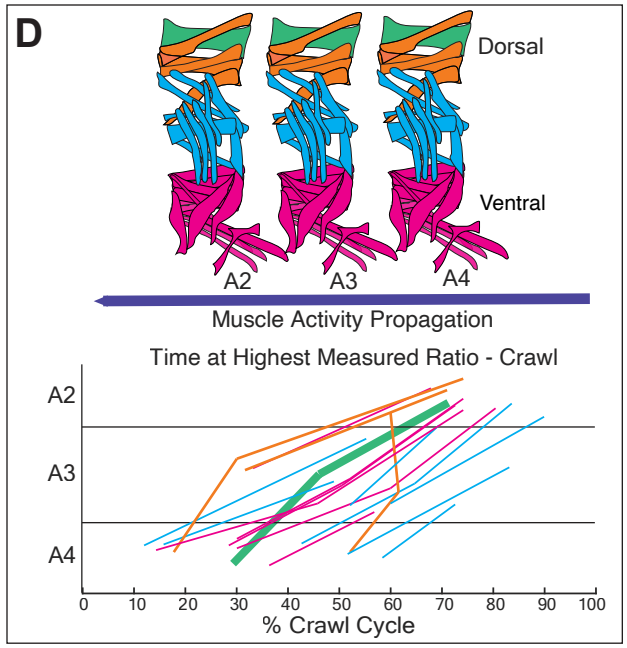
D
Dorsal
Ventral
A2
A3
A4
Muscle Activity Propagation
Time at Highest Measured Ratio - Crawl
A2
A3
A4
0
10
20
30
40
50
60
70
80
90
100
% Crawl Cycle

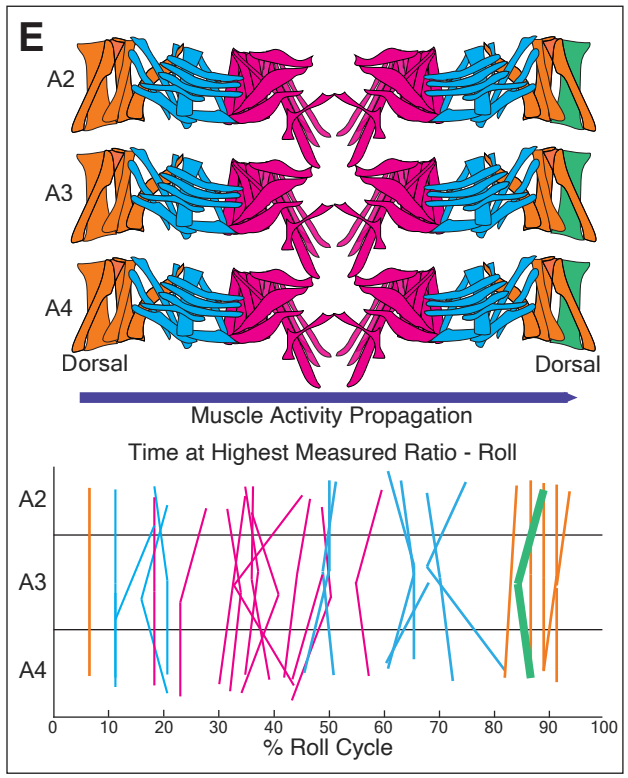
E
A2
A3
A4
Dorsal
Dorsal
Muscle Activity Propagation
Time at Highest Measured Ratio - Roll
A2
A3
A4
0
10
20
30
40
50
60
70
80
90
100
% Roll Cycle

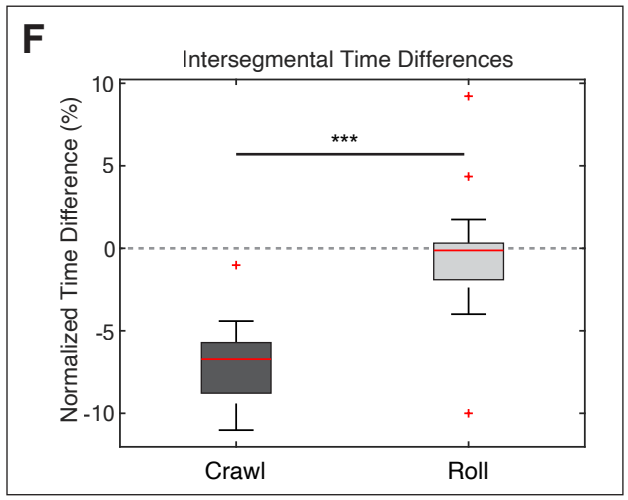
F
Intersegmental Time Differences
Normalized Time Difference (%)
10
5
0
-5
-10
***
Crawl
Roll

Figure 1: Muscles demonstrate a segmentally synchronous, circumferential wave of activity during escape (**A**) Schematic illustrating four patterns of escape observed, based on combination of which side larva bends toward (left or right) and which direction the larva rotates (clockwise or counterclockwise). Translation direction is determined by direction of rotation. Histogram shows frequency of escape patterns observed in response to sustained optogenetic Goro activation (light gray, n = 64 rolls) or in response to global heat + vibration stimulus (dark gray, n = 47 rolls). (**B**) SCAPE dual-color stills from single roll bout, showing same muscle appearing in focal plane simultaneously across segments. Muscle GCaMP increased primarily on the bent side of the larva. Arrow indicates direction of larval rotation. (**C**) Confocal dual-color stills from single crawl bout in larva, demonstrating increase in GCaMP brightness from posterior to anterior muscles during single crawl bout. (**D**) Schematic of muscle arrangement in three neighboring hemisegments, color coded by general dorsal, lateral and ventral muscle groups. Blue arrow indicates posterior-to-anterior propagation of muscle activity. Peak ratiometric muscle fluorescence times during single crawl bout across three segments. During forward crawling, muscles of segment A4 reach peak activity before A3, and muscles of segment A3 reach peak activity before A2 segment, demonstrating the propagation of peristaltic contraction from posterior to anterior segments. Representative homologous muscle across hemisegments and peak activity lines in green for clarity of segmental propagation of activity during crawling. (**E**) Three-segment schematic of hemisegments, color coded by general dorsal, lateral and ventral muscle groups. Blue arrow indicates circumferential propagation of muscle activity. Highest observed ratiometric muscle fluorescence times during single roll cycle with SCAPE across segments A2-A4. Same muscle types across segment A2 to A4 simultaneously reach their peak activity. Muscles are color-coded according to panel **D**, demonstrating dorsal to ventral to dorsal (circumferential) propagation of muscle contraction. Representative homologous muscle across segments and peak activity lines in green indicate an example of segmental synchrony of activity during rolling. (**F**) Comparison between time difference of muscles in segments A2-A4 for forward crawling versus rolling (crawl: n = 2 crawls, 2 larvae, 86 muscles; roll: n = 4 rolls, 3 larvae, 372 muscles). Negative values indicate that muscles in A4 are active before muscles in A2 and "0" indicates synchronous contraction. Mann-Whitney U tests were performed between intersegmental roll lag values and intersegmental crawl lag values. P values are indicated as ***$p<0.001$. Scale bars = 100µm (B), 50µm (C).

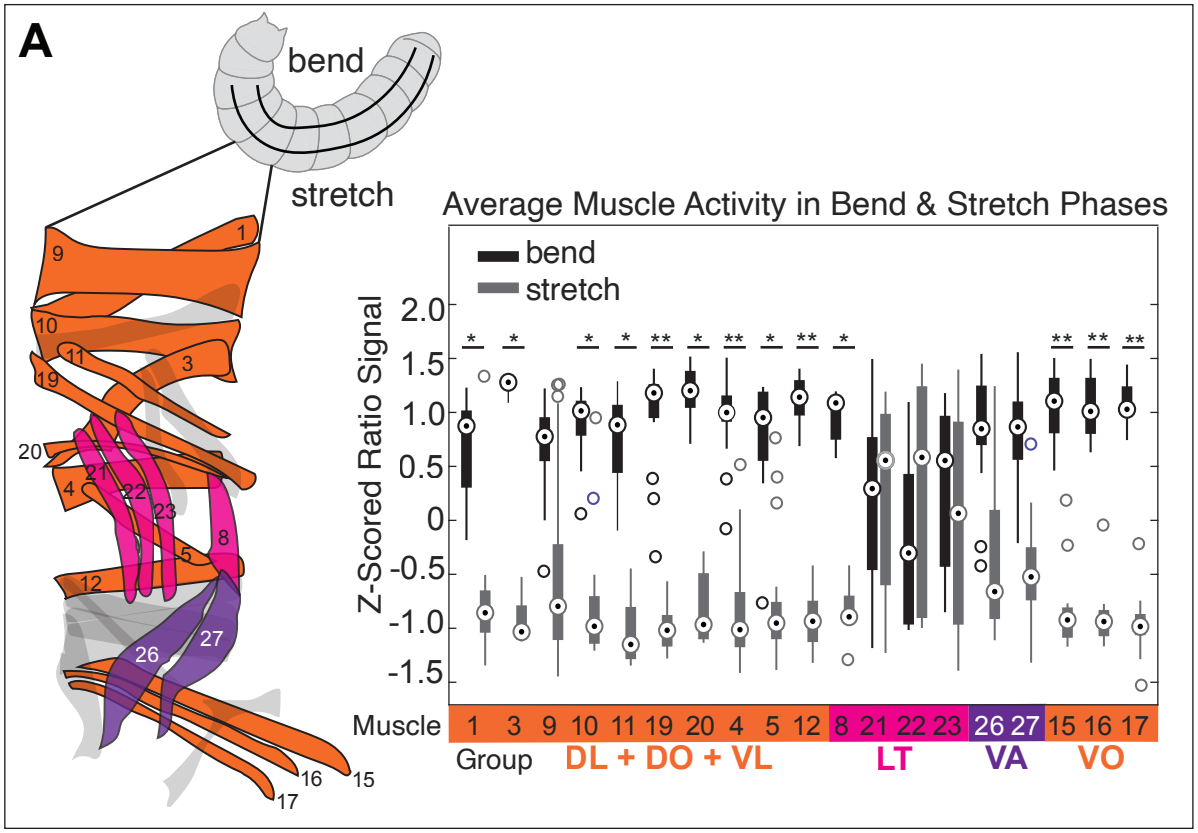
A
bend
stretch
Average Muscle Activity in Bend & Stretch Phases
bend
stretch
Z-Scored Ratio Signal
2.0
1.5
1.0
0.5
0
-0.5
-1.0
-1.5
Muscle
1 3 9 10 11 19 20 4 5 12 8 21 22 23 26 27 15 16 17
Group
DL + DO + VL
LT
VA
VO

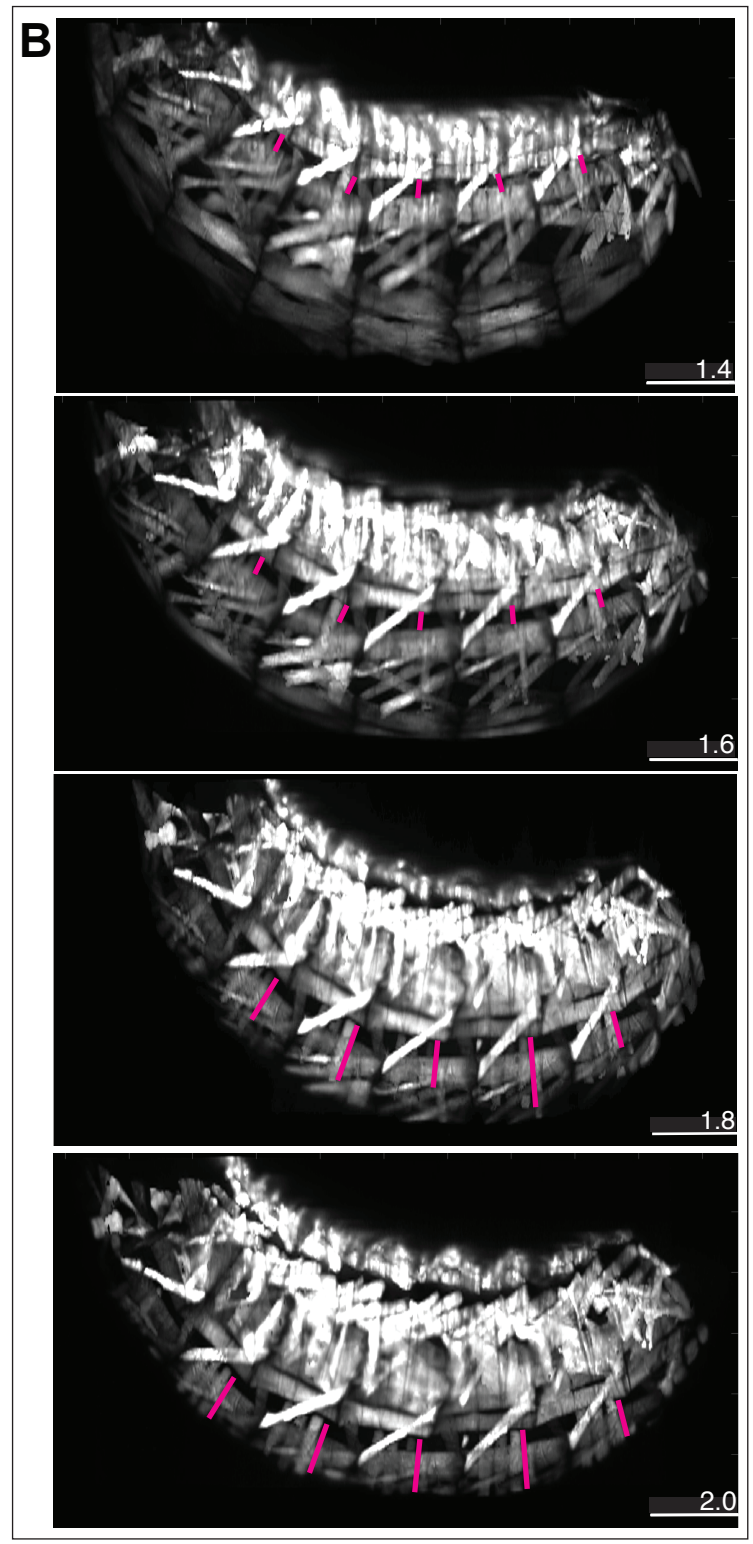
B
1.4
1.6
1.8
2.0

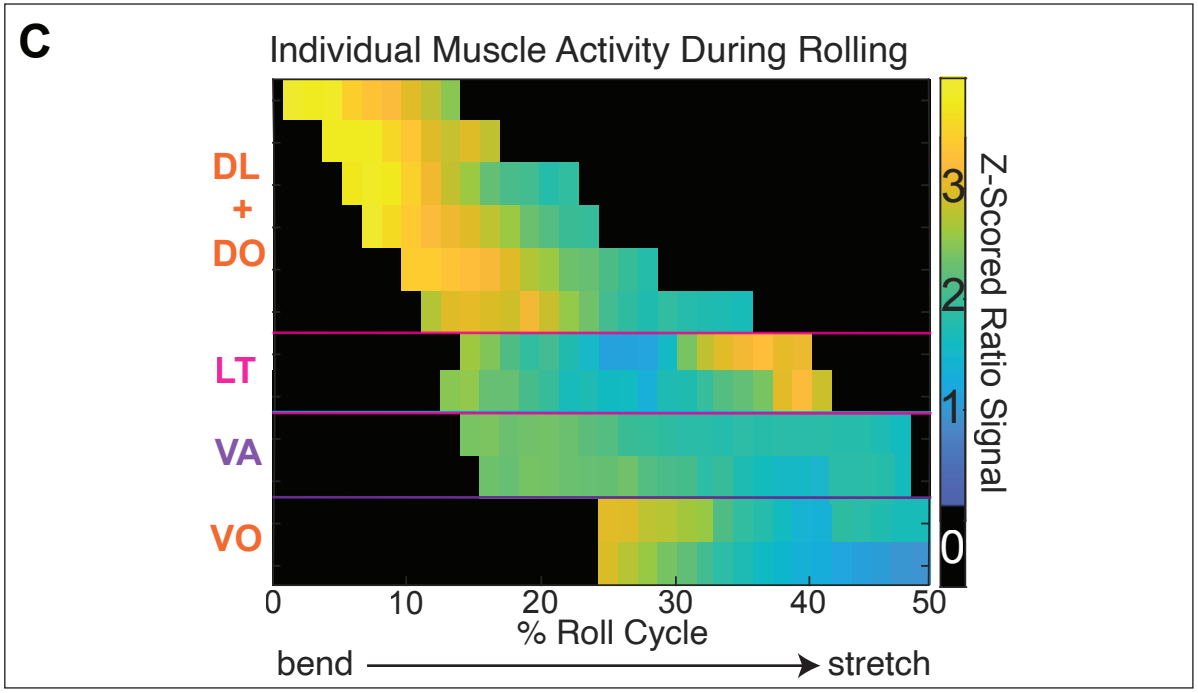
C
Individual Muscle Activity During Rolling
DL
+
DO
LT
VA
VO
Z-Scored Ratio Signal
3
2
1
0
0
10
20
30
40
50
% Roll Cycle
bend
stretch

Figure 2: Intrasegmental muscle activity patterns demonstrate functional antagonism during escape. (**A**) Hemisegment schematic of example measured muscles color-coded according to activity pattern (*left*). Boxplot showing mean z-scored ratio signal for individual muscles from frames when muscles were along the bent side of the larva (black) vs. along the stretched side of the larva (gray) (*right*). Data are grouped and color-coded along x-axis according to similarity of activity patterns. Orange muscles (dorsal longitudinal, DL; dorsal oblique, DO; ventral longitudinal, VL; ventral oblique, VO) show increased ratio signal along the bent side of the larva, while magenta (lateral transverse, LT) muscles show on average equivalent ratiometric signal on bent and stretched sides. Purple (ventral acute, VA) muscles show elevated activity on bent side, but the difference between activity in bent and stretched sides is insignificant. (n = 3 rolls, 3 larvae, 280 muscles). (**B**) Example ratiometric SCAPE stills of larval escape. Magenta lines highlight lateral transverse (LT) muscles, demonstrating low ratio signal while rotating out of the bend and increased ratio signal while rotating toward the stretched side of the larva. (**C**) Heatmap of z-scored ratio signal across individually measured example muscles, organized from dorsal (top row) to ventral (bottom row). LT ratiometric traces show increased activity while rotating toward the bend, an activity pattern different from other muscles. Color bar to the right of shows range of z-scored ratio signal values. Black indicates frames when muscles were out of the FOV and not measured. Scale bars = 100µm.

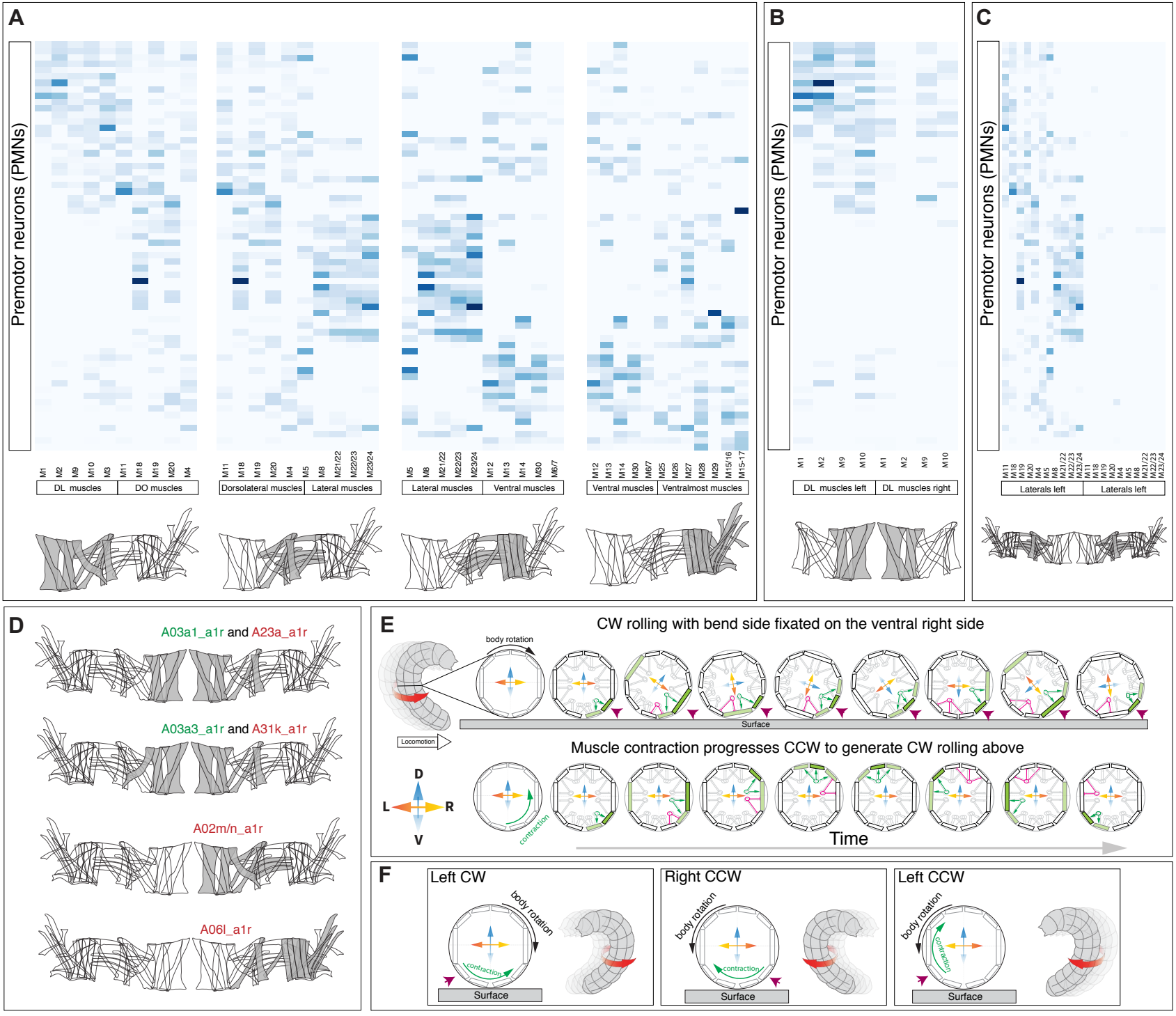
A
Premotor neurons (PMNs)
M1 M2 M9 M10 M3 M11 M18 M19 M20 M4
DL muscles
DO muscles
M11 M18 M19 M20 M4 M5 M8 M21/22 M22/23 M23/24
Dorsolateral muscles
Lateral muscles
M5 M8 M21/22 M22/23 M23/24 M12 M13 M14 M30 M6/7
Lateral muscles
Ventral muscles
M12 M13 M14 M30 M6/7 M25 M26 M27 M28 M29 M15/16 M15-17
Ventral muscles
Ventralmost muscles
B
Premotor neurons (PMNs)
M1 M2 M9 M10 M1 M2 M9 M10
DL muscles left
DL muscles right
C
Premotor neurons (PMNs)
M11 M18 M19 M20 M4 M5 M8 M21/22 M22/23 M23/24 M11 M18 M19 M20 M4 M5 M8 M21/22 M22/23 M23/24
Laterals left
Laterals left
D
A03a1_a1r and A23a_a1r
A03a3_a1r and A31k_a1r
A02m/n_a1r
A06l_a1r
E
CW rolling with bend side fixated on the ventral right side
body rotation
Surface
Locomotion
Muscle contraction progresses CCW to generate CW rolling above
D
L
R
V
contraction
Time
F
Left CW
body rotation
contraction
Surface
Right CW
body rotation
contraction
Surface
Left CW
body rotation
contraction
Surface

Figure 3

Figure 3: Premotor circuit organization for circumferential progression of muscle activity observed during escape. (**A-C**) Heat maps representing the normalized weighted-synaptic output (blue shading) of left PMN (rows) onto different subsets of left MNs (columns). Grayed sketches at the bottom of heatmaps indicate the target muscles of MNs in heatmap. (**A**) PMNs demonstrate connectivity patterns with dorsoventral organization, where PMNs presynaptic to DL MNs also establish synapses with MNs innervating the neighboring DO muscles (left), PMNs presynaptic to dorsolateral MNs also establish synapses with MNs innervating the neighboring lateral muscles (second from left), PMNs presynaptic to lateral MNs also establish synapses with MNs innervating the neighboring ventral muscles (second from right), and PMNs presynaptic to ventral MNs also establish synapses with MNs innervating the neighboring ventralmost muscles (right). (**B**) Left PMNs presynaptic to left DL MNs also establish significant number of synapses with right DL MNs. Left and right DL muscles span neighboring regions along the dorsal body midline. (**C**) Left PMNs presynaptic to left lateral/dorsolateral MNs have negligible connectivity with right DL MNs. Lateral/dorsolateral on the left and right side are spatially distant from each other. **(D)** Individual PMNs tend to synapse with MNs that correlate with spatially proximal muscles. The first two example diagrams demonstrate connectivity motifs of overlapping excitatory (green) and inhibitory (red) drive to the same muscles, providing a mechanism for precise temporal control of contraction. The second two example diagrams show two putative inhibitory PMNs that synapse with MNs that innervate spatially proximal lateral and ventral muscles, respectively. **(E)** Schematic model showing that to generate clockwise rolling (top panel), muscle contraction progresses counterclockwise (low panel). Circles are cross-section depictions of a larva at different time points. Rectangular shapes around the circumference indicate the body wall muscles. Dark and light green indicate the fully and partially contracted muscles, respectively. Purple arrowheads indicate the fixated bend sides in the top panel. The dorsoventral axis rotates clockwise in the top panel, while it is fixated at the bottom panel. The green and magenta oval shapes indicate the excitatory and inhibitory inputs from active PMNs, respectively. Gray oval shapes indicate inactive PMNs. **(F)** Schematic showing the opposite direction of contraction progression (green arrow) and body rotation (black arrow) in three different roll types not described in panel (E). Note the different location of bend side (purple arrow) in left and right CCW rolls.

A

Motor neurons	Target Muscles
(Ib) MN1	1
(Ib) MN2	2
(Ib) MN3	3
(Ib) MN4	4
(Ib) MN9	9
(Ib) MN10	10
(Ib) MN11	11
(Ib) MN19	19
(Ib) MN20	20
(Ib) MN5	5
(Ib) MN6/7	6/7
(Ib) MN12	12
(Ib) MN13	13
(Ib) MN14	14
(Ib) MN30	30
(Ib) MN26	26
(Ib) MN27	27
(Ib) MN29	29
(Ib) MN15/16	15/16
(Ib) MN15/16/17	15/16/17
(Ib) MN28	28
(Ib) MN8	8
(Ib) MN21/22	21/22
(Ib) MN22/23	22/23
(Ib) MN23/24	23/24
(Ib) MN18	18
(Ib) MN25	25
(Is) MNISN	1/2/3/4/9/10/11/19/20
(Is) MNISNb/d	6/7/12/13/14/15/16/30

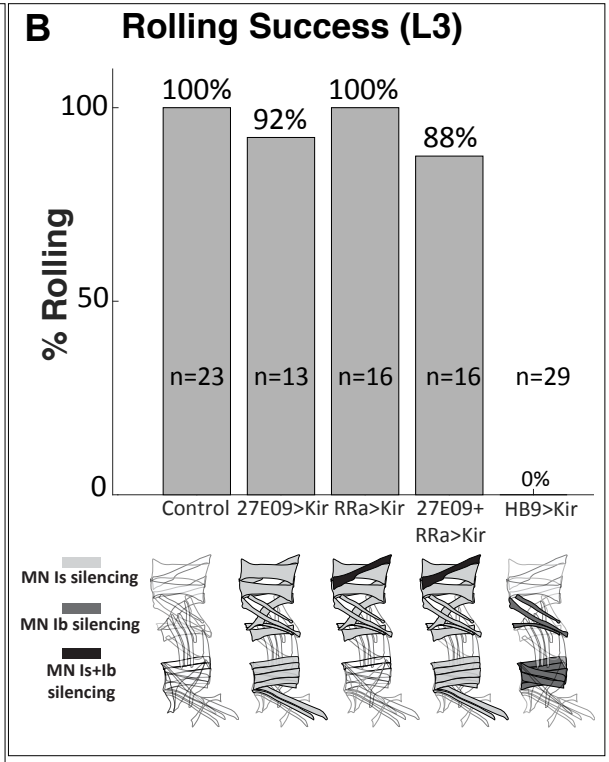

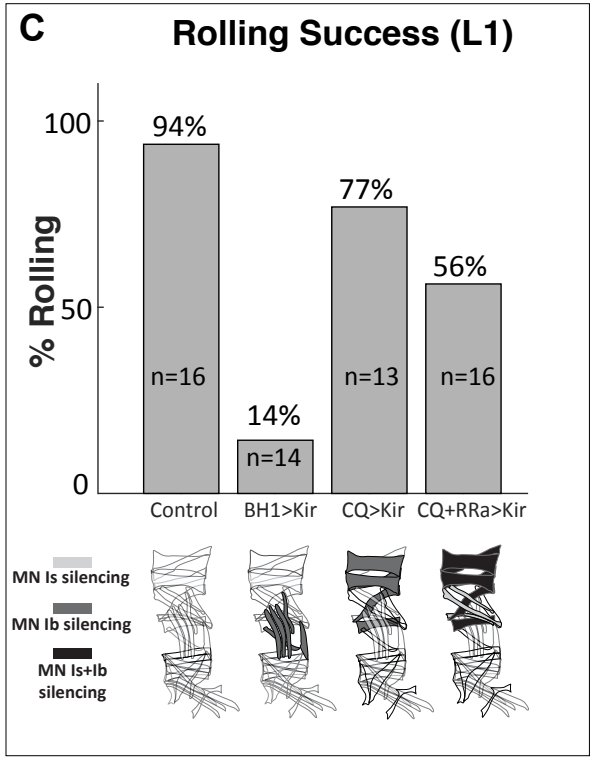

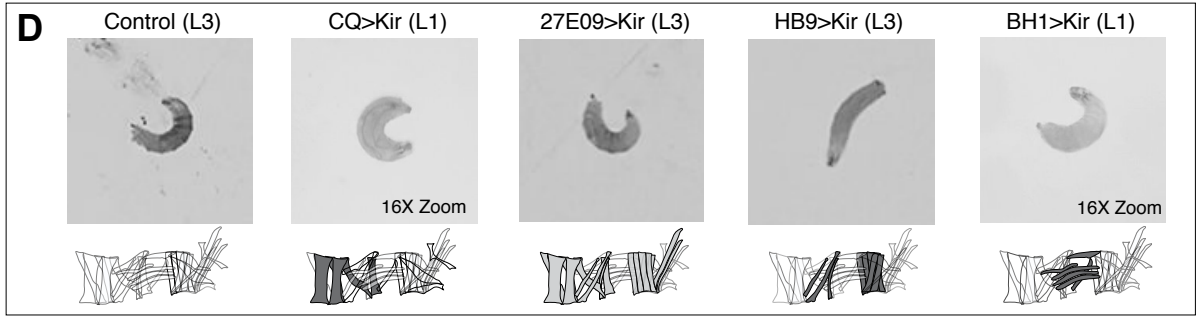

Figure 4

Figure 4: Silencing different MN groups leads to different forms of defects in rolling. (**A**) The proportion of L3 animals able to complete at least one complete roll. Silencing Is MNs alone (27E09>Kir) or in combination with a single Ib MN (RRa>Kir and 27E09+RRa>Kir) had little or no effect on rolling performance. Silencing Ib MNs innervating ventral longitudinal and dorsal oblique muscles (HB9>Kir) leads to complete failure in rolling. Control animals are 69E06-LexA/+; Aop-Chrimson-mCherry, UAS-Kir2.1/+, while each MN silencing group carries one or two MN-Gal4 components. N = 23 larvae for control, 13 for 27E09>Kir, 16 for RRa>Kir, 16 for 27E09+RRa>Kir, 29 for HB9>Kir. The cartoon below each histogram bar shows the muscles groups whose Ib (light gray), Is (dark gray), or both Ib and Is inputs are silenced.

(**B**) Silencing lateral transverse muscles with BH1>Kir greatly impaired rolling, as 12 out of 14 BH1>Kir animals were unable to complete even a single roll. Silencing Ib MNs innervating dorsal muscles (CQ>Kir) lead to a milder reduction in rolling success rate than combinatorial silencing of Ib and a single Is MN (CQ+RRA>Kir). N = 16 animals for control, 14 for BH1>Kir, 13 for CQ>Kir, 16 for CQ+RRa>Kir, 29 for HB9>Kir.

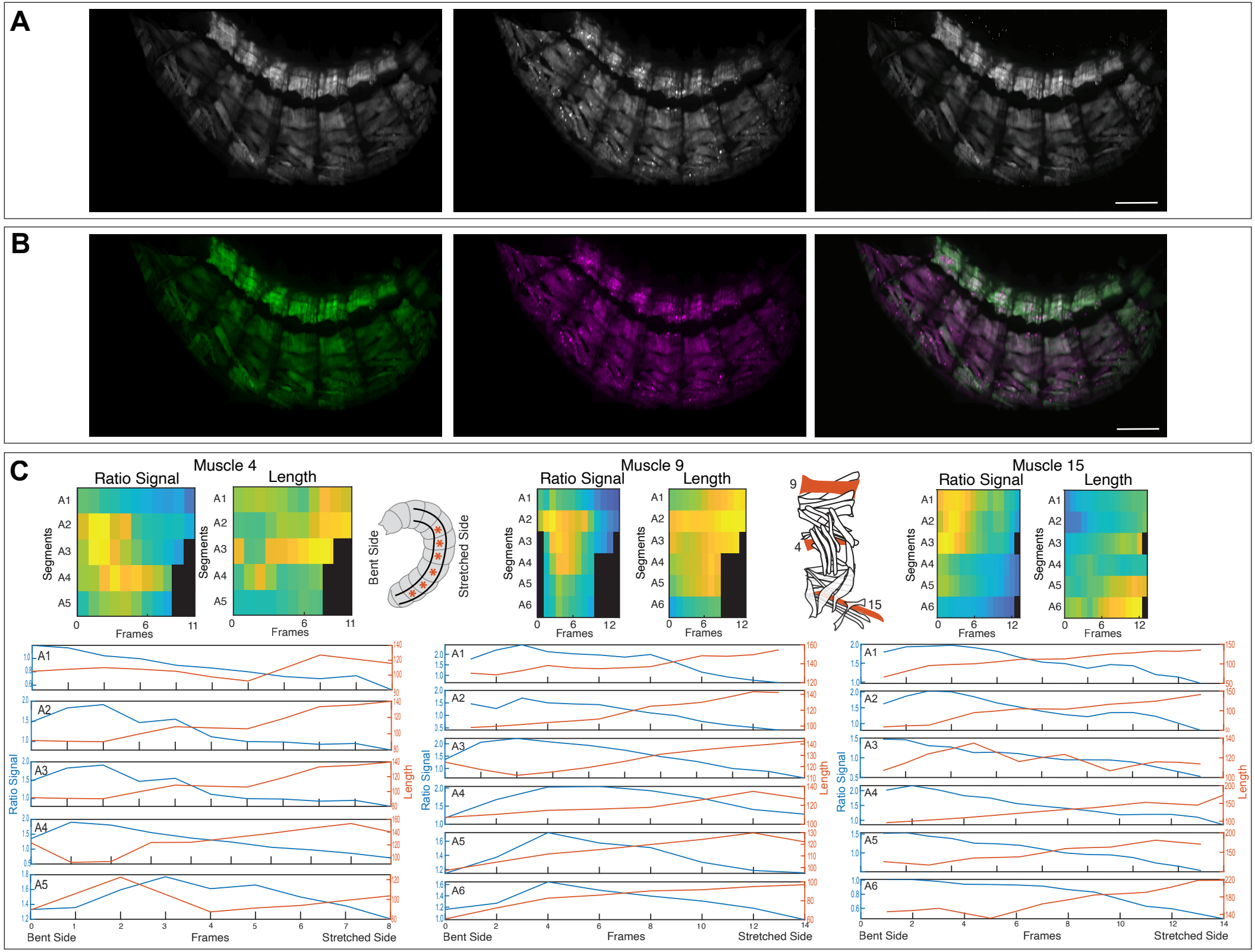
A
B
C
Muscle 4
Ratio Signal
Length
Segments
A1
A2
A3
A4
A5
Frames
Bent Side
Stretched Side
Muscle 9
A6
9
4
15
Muscle 15
Ratio Signal
Length
Bent Side
Frames
Stretched Side

Supplemental Figure 1: Dual-color SCAPE permits quantitation of individual muscle activities across larval segments during escape. (**A,B**) Example stills from GCaMP, mCherry, and calculated ratiometric SCAPE images in grayscale (**A**) and in respective green and magenta and merged (**B**). (**C**) Heatmaps of ratiometric signal and length measurements extracted from example muscles 4 (left), 9 (middle), and 15 (right) across segments A1-A6 during escape rolling. Schematics indicate segments measured and example muscles measured. Below, ratiometric signals (blue) and length measurements (orange) extracted from example muscles during rolling. Plots demonstrate inverse relationship between ratiometric signal and muscle length, demonstrating that ratiometric signal serves as adequate quantitation of muscle contraction.

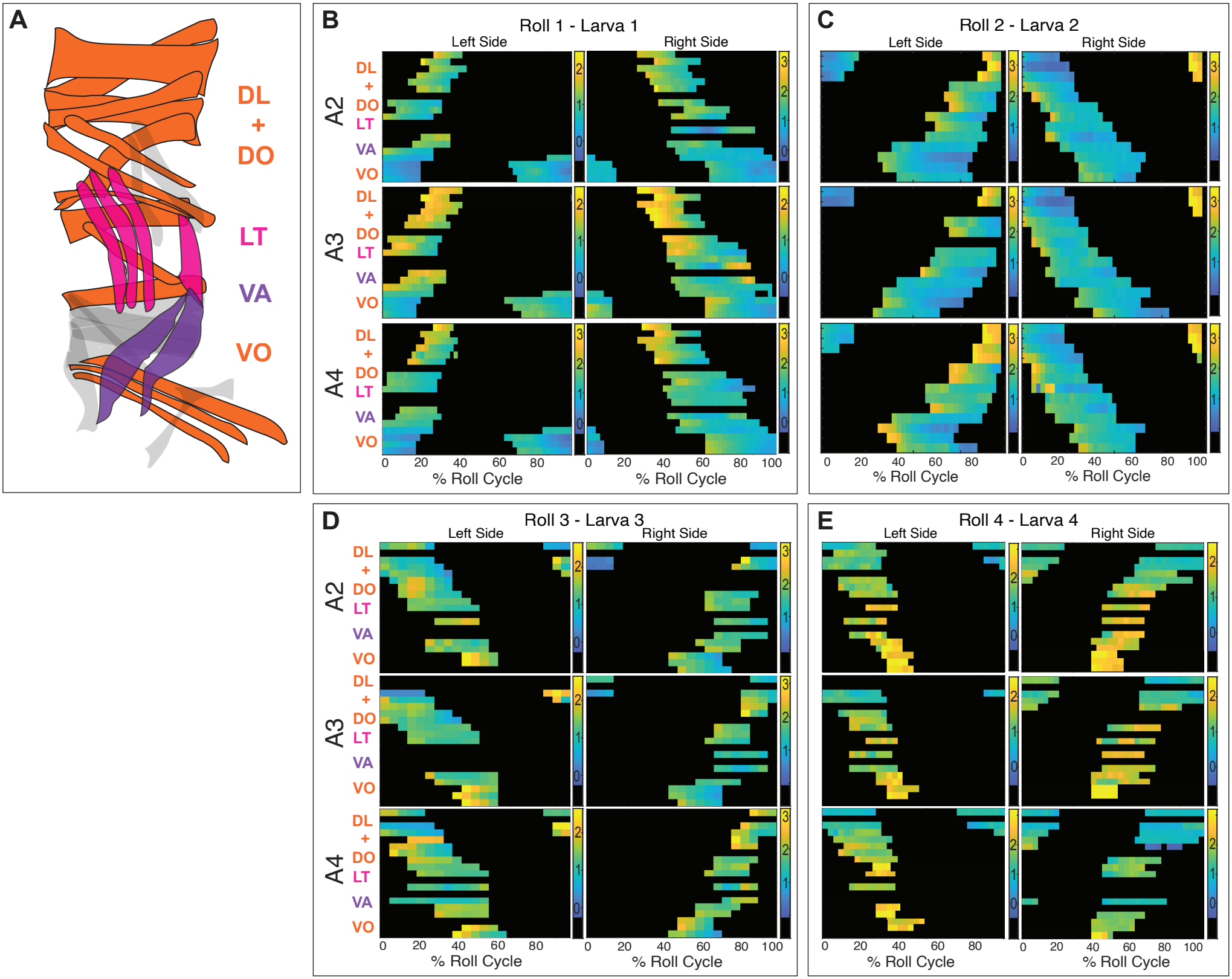
A
DL
+
DO
LT
VA
VO
B
Roll 1 - Larva 1
Left Side
Right Side
A2
A3
A4
DL
+
DO
LT
VA
VO
0 20 40 60 80
0 20 40 60 80 100
% Roll Cycle
% Roll Cycle
C
Roll 2 - Larva 2
Left Side
Right Side
D
Roll 3 - Larva 3
Left Side
Right Side
E
Roll 4 - Larva 4
Left Side
Right Side

Supplemental Figure 2: Individual muscle activity patterns show symmetric dorsoventral propagation on left and right sides. (A) Hemisegment color-coded by muscle groups that correspond with color-coded muscle labels to the left of the rows in heatmaps. These color groupings match the population bend vs. stretch fluorescence comparisons in Figure 2A. **(B-E)** Heatmaps of z-scored ratiometric signal across all measured muscles, divided by segment (A2-A4) and side (left and right). Each row for each heatmap panel is an individual muscle, organized from dorsal (top row) to ventral (bottom row), and color-coded according to muscle groupings in A. Colorbars to the right of the upper heatmaps show range of ratiometric values. **(B-D)** Traces from muscles moving out of the bend during rolling show moderate decrease in ratiometric signal. **(E)** Muscles moving toward the bend show mild increase in ratiometric signal. Notably, ratiometric signals in muscles moving into the bend from our imaging perspective have a less apparent activity pattern.

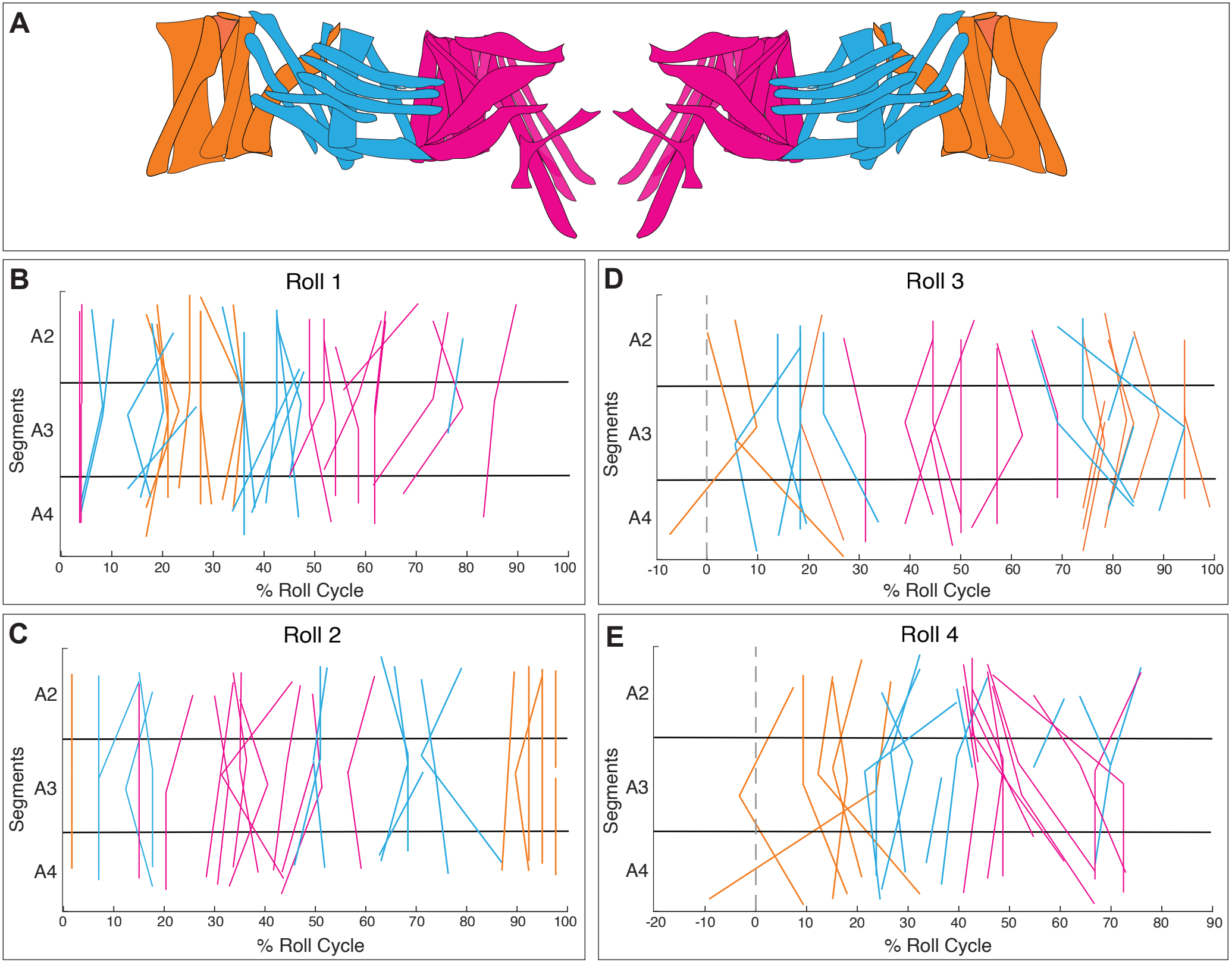
A
B
Roll 1
A2
A3
A4
Segments
0
10
20
30
40
50
60
70
80
90
100
% Roll Cycle
C
Roll 2
A2
A3
A4
Segments
0
10
20
30
40
50
60
70
80
90
100
% Roll Cycle
D
Roll 3
A2
A3
A4
Segments
-10
0
10
20
30
40
50
60
70
80
90
100
% Roll Cycle
E
Roll 4
A2
A3
A4
Segments
-20
-10
0
10
20
30
40
50
60
70
80
90
% Roll Cycle

Supplemental Figure 3: Muscle activities occur as segmentally synchronous dorsoventral propagation. (A) Segment color-coded by spatial muscle groups (dorsal, lateral, and ventral) that correspond with color-coded muscle activity peak lines in subsequent panels. **(B-E)** Highest measured ratiometric muscle fluorescence times during single rolls (n = 4 rolls, 4 larvae). Note that, because rolling is a cyclical behavior, axes were adjusted in panels **D,E** to illustrate relative synchrony in segments where select muscles that appear twice during a single roll have offset peaks in linear time of a single roll.

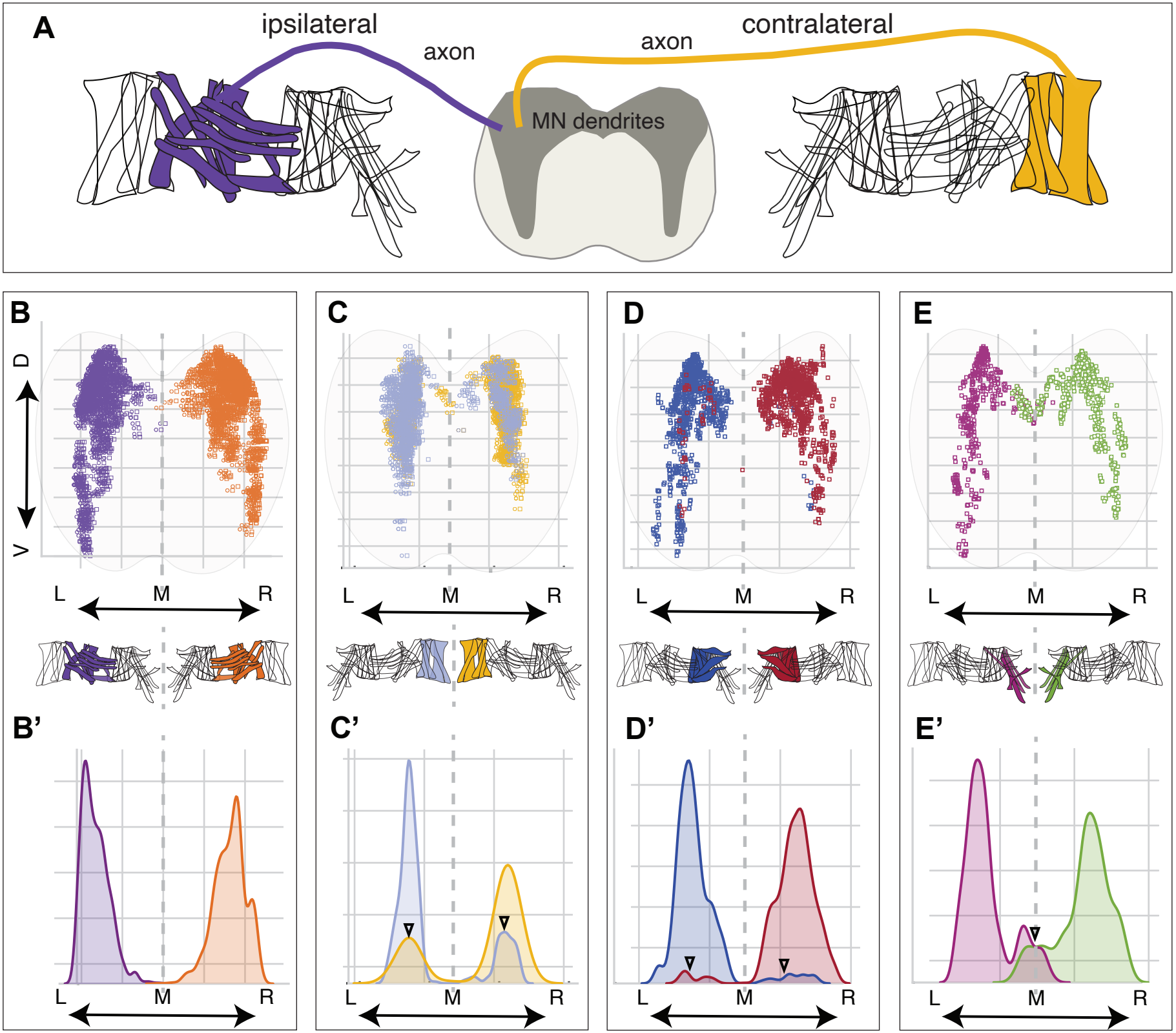
A
ipsilateral
axon
axon
contralateral
MN dendrites
B
D
V
L
M
R
B'
C
C'
D
D'
E
E'

Supplemental Figure 4: Left and right midline muscles receive inputs from partially overlapping regions of neuropil. (A) Schematic showing motor neurons whose dendrites receive postsynaptic input either ipsilateral or contralateral to their axon projections. (**B-E**) Dorsoventral and mediolateral distributions of postsynaptic sites on MNs innervating the muscle groups indicated below each panel. Shaded gray area represents the cross-sectional view of the neuropil. Gray dashed lines define the midline (M) dividing the neuropil into left (L) and right (R) hemisegments, and the midline of dorsal and vental body wall muscles, respectively. (**B**) Postsynaptic sites of MNs innervating lateral muscles are localized exclusively in either left or right hemisegment of the neuropil. (**C-E**) Postsynaptic sites of MNs innervating muscles near the dorsal or ventral midlines occupy partially overlapping regions of the neuropil. (**B'-E'**) 1D kernel density plot of MN postsynaptic sites on the mediolateral axis. Black arrowheads in **C'-E'** show overlapping localization of postsynaptic sites of left and right MNs.

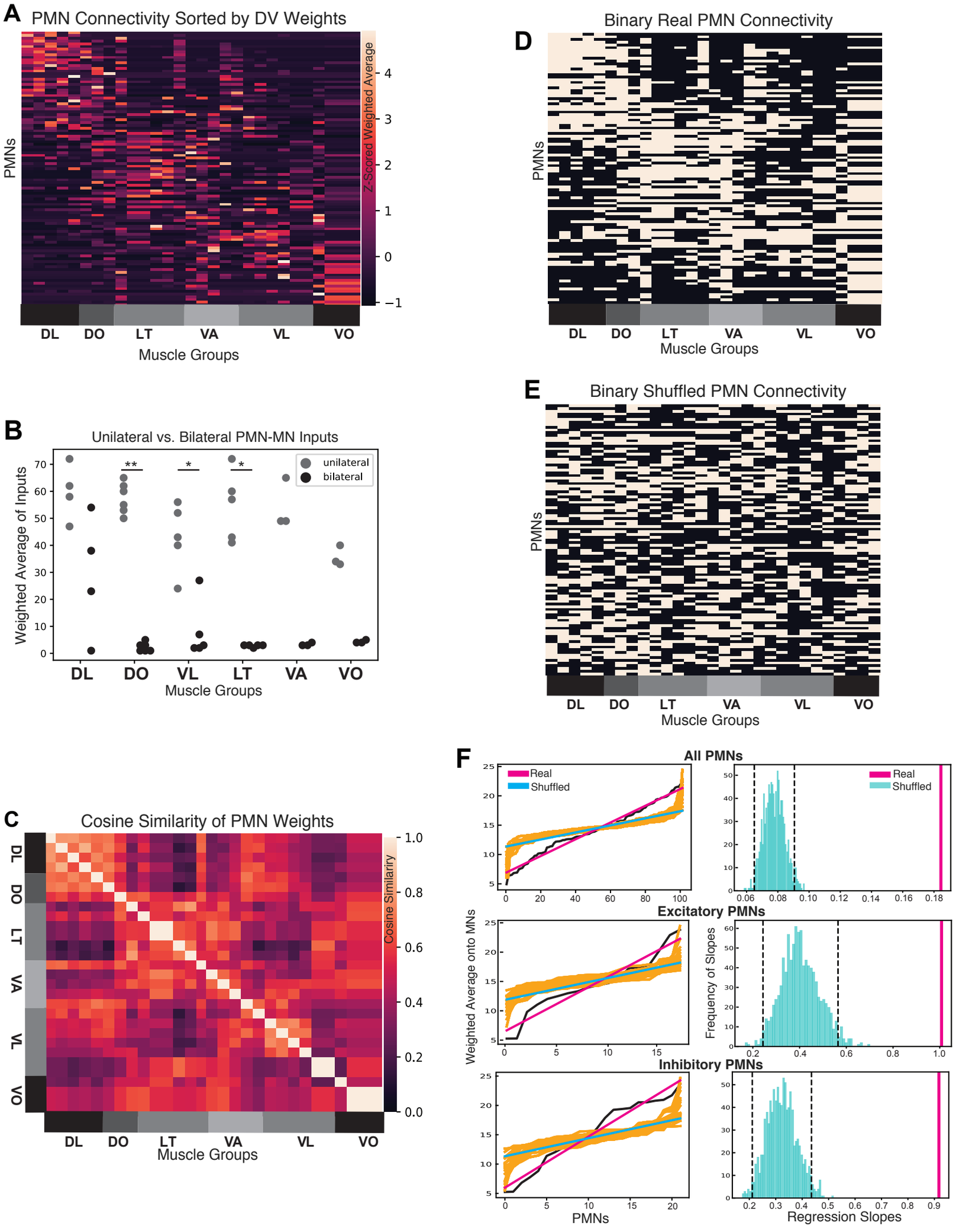
A
PMN Connectivity Sorted by DV Weights
PMNs
Z-Scored Weighted Average
4
3
2
1
0
−1
DL
DO
LT
VA
VL
VO
Muscle Groups
B
Unilateral vs. Bilateral PMN-MN Inputs
Weighted Average of Inputs
unilateral
bilateral
**
*
*
DL
DO
VL
LT
VA
VO
Muscle Groups
C
Cosine Similarity of PMN Weights
Cosine Similarity
1.0
0.8
0.6
0.4
0.2
0.0
DL
DO
LT
VA
VL
VO
Muscle Groups
D
Binary Real PMN Connectivity
PMNs
DL
DO
LT
VA
VL
VO
Muscle Groups
E
Binary Shuffled PMN Connectivity
PMNs
DL
DO
LT
VA
VL
VO
Muscle Groups
F
All PMNs
Real
Shuffled
Excitatory PMNs
Inhibitory PMNs
Weighted Average onto MNs
Frequency of Slopes
PMNs
Regression Slopes

Figure S5: Premotor circuit organization supports circumferential muscle contraction sequence. (**A**) Heatmap of synaptic weights of PMNs onto MNs, averaged across left and right PMNs and MNs and z-scored. PMNs (rows) are sorted by their weighted average onto MNs arranged dorsoventrally, illustrating that the PMN output onto MNs shows a global organization that permits muscle contraction in a dorsoventral sequence, as occurs in the circumferential muscle wave during rolling. (**B**). Quantitative comparison of PMN unilateral and bilateral projections onto MNs innervating specific spatial muscle subgroups. Each point represents the weighted average of PMN inputs onto a specific muscle within the muscle subgroup indicated on the x-axis. Mann-Whitney U tests were performed between weighted averages of PMNs onto unilaterally vs. bilaterally to MNs, demonstrating significant differences between unilateral vs. bilateral premotor innervation of muscle groups farther from the midline (DO, VL, and LT) and insignificant differences between muscle groups closer to the midline (DL, VA, and VO), providing a circuit structural correlate for premotor drive of circumferential muscle contractions in rolling. P values are indicated as *$p<0.05$, **$p<0.01$. (**C**) Cosine similarity of PMN inputs to MNs organized in dorsoventral order demonstrates that MNs innervating muscle groups that are closer together in dorsoventral axis have a high degree of shared input from PMNs. (**D**) Binarized synaptic weights of PMNs onto MNs organized dorsoventrally, as in (A). (**E**) Example of shuffled binary synaptic weights from PMNs onto MNs, where connections from PMNs onto specific MNs were randomly selected while preserving the total number of outputs from each PMN and the probability of input onto each MN. Notably, the shuffling procedure, despite preserving global statistics of PMN outputs and MN inputs, noticeably removes the dorsoventral preferences of real PMNs observed in (A) and (D). (**F**) (Left) Quantitative comparison of weighted averages of PMNs onto MNs arranged in dorsoventral order from binary real PMN-MN connectome data (as in (D)) vs. 1000 binary shuffled PMN-MN connectivity matrices (as in example (E)). Real weighted average of PMNs onto MNs for all PMNs (top), PMNs previously identified as excitatory (middle), and PMNs previously identified as inhibitory (bottom) is shown in black, with corresponding regression line in magenta. Weighted averages from 1000 randomly shuffled PMN-MN matrices shown in gold, with corresponding mean regression line across all shuffles in cyan. Regression lines of real PMN-MN weighted averages for all PMNs, excitatory-only PMNs, and inhibitory-only PMNs demonstrate steeper slopes (higher regression coefficients) than that of the shuffled PMN-MN weighted averages, highlighting their stronger dorsoventral spatial preference than given by chance. (Right) Histograms illustrating frequency of regression coefficients over 1000 shuffled PMN-MN matrices (cyan). Real-valued regression coefficient (magenta) falls well outside of the 95% confidence bounds of the distribution of shuffled regression coefficients (black dashed lines), indicating that dorsoventral structure of PMN-MN connectivity is significantly different from chance.